UNIVERSITY OF OKLAHOMA

GRADUATE COLLEGE

MULTI-RADAR ANALYSIS OF THE 20 MAY 2013 MOORE, OKLAHOMA SUPERCELL THROUGH TORNADOGENESIS AND INTENSIFICATION

A THESIS

SUBMITTED TO THE GRADUATE FACULTY

in partial fulfillment of the requirements for the

Degree of

MASTER OF SCIENCE IN METEOROLOGY

By

CLARICE N. SATRIO
Norman, Oklahoma
2019

MULTI-RADAR ANALYSIS OF THE 20 MAY 2013 MOORE, OKLAHOMA SUPERCELL THROUGH TORNADOGENESIS AND INTENSIFICATION

A THESIS APPROVED FOR THE
SCHOOL OF METEOROLOGY

BY THE COMMITTEE CONSISTING OF

Dr. Robert D. Palmer, Chair

Dr. David J. Bodine, Co-Chair

Dr. Pierre E. Kirstetter

Dedication

This thesis is dedicated to the memory of my grandpa, Floyd Moerbe. Thank you for all the life advice and memories you shared with me.

Acknowledgments

Funding for this research was supported by Nanowave Technologies Inc and NSF grant AGS-1823478. Special thanks to my advisors, Dr. David Bodine and Dr. Robert Palmer for their mentorship and guidance in the completion of this thesis. Your encouragement and motivation throughout the project pushed me through difficult and challenging times, and shaped me into a better researcher. I also thank Dr. Pierre Kirstetter for taking the time to serve as a committee member and for providing insightful feedback that led to the improvement of this thesis, and Dr. Boonleng Cheong and Charles Kuster for graciously providing PX-1000 and KOUN data.

My graduate experience and the completion of this thesis was truly a culmination of support and encouragement from friends and family, without which this achievement would not have been possible. Thanks to the School of Meteorology faculty and staff for taking a chance on me and challenging me, academically and personally, throughout this rigorous program which made me a better student and researcher. The advice and lessons I was taught are invaluable. To friends, those near and far, thanks for reminding me that life exists beyond graduate school. Thanks to my family, especially my mom and dad, for providing me with all the opportunities to succeed in life. Your love and support has been a constant presence in my life and for that I'm grateful. To my two dogs, Cali and Kira, who love me unconditionally and are always there to keep me sane by driving me insane. Last but not least, I want to thank Martin Satrio for being the best husband a wife could ever ask for. I'm beyond lucky to have shared my undergraduate and graduate experiences with

you, celebrating in times of triumph and comforting each other in times of hardship. Thanks for always believing in me when it was hard to believe in myself. I hope to one day to have the confidence in myself that you have in me.

Table of Contents

List Of Tables

List Of Figures

Abstract

On 20 May 2013, a violent, long-track EF-5 tornado impacted Moore, Oklahoma and surrounding areas, occurring within a network of radars operating in close proximity to the supercell. This network of radars consisted of three WSR-88Ds – KTLX, KOUN, and KCRI, in addition to the PX-1000, a rapid-scan, transportable, X-band radar with 20-s temporal resolution. This analysis focused on detailing polarimetric supercell attributes leading up to tornadogenesis and through tornado intensification. Two analyses were conducted to analyze in-storm processes within the supercell high-spatiotemporal supercell evolution using PX-1000 and volumetric characteristics of Z_{DR} and K_{DP} signatures using KTLX and KOUN.

High-temporal observations from PX-1000 resolved three distinct rear-flank downdraft (RFD) surges, two of which occurred prior to tornadogenesis (1946:09 and 1952:27 UTC) and one coincident with tornadogenesis (1957:05 UTC). The RFD surges were characterized by transient intensifications in ΔV_{max}, an advancing Z_H gradient wrapping cyclonically around the low-level mesocyclone, and a decrease in ρ_{hv} within the hook echo, likely resulting from the lofting of light debris from increased wind speeds. The second and third RFD surges are especially robust, with ΔV_{max} exceeding "tornado" threshold (≥ 40 m s^{-1}) and detection of a tornado debris signature utilizing a hydrometeor classification algorithm. Patterns associated with the RFD surges suggests the possibility of brief, weak tornadoes occurring prior to tornadogenesis (1956 UTC), but ultimately resulting in the failure of the tornadoes to sustain themselves.

Trends in Z_{DR} arc and K_{DP} foot volumetric characteristics as well as Z_{DR} and K_{DP} columns are also documented using KTLX and KOUN. In the times leading up to tornadogenesis, while Z_{DR} arc remained relatively shallow, K_{DP} foot exhibited consolidation / deepening immediately downshear of the updraft, indicating increased likelihood of tornadogenesis. Additionally, prior to tornadogenesis, Z_{DR} and K_{DP} columns displayed a decrease in both depth and volumetric extent, signifying a weakening updraft as a result of a strengthening downward-directed perturbation pressure gradient force. Contrary to an overall weakening trend prior to tornadogenesis, column analysis detected an updraft pulse at $\sim$1942 UTC. Lastly, the steady decrease in column strength shifts to rapid growth just before (5 – 10 min after) tornadogenesis for K_{DP} (Z_{DR}) column.

Chapter 1

Introduction

Observational and numerical studies have made considerable progress in diagnosing and understanding supercell environments and dynamics. The environmental conditions that are conducive for supercells are well understood, and thus convective-allowing short-term model guidance has drastically improved forecasting. The lower-tropospheric profiles of temperature, humidity, and winds have been found to be the most important parameters for the formation and maintenance of supercells (Rasmussen and Blanchard 1998; Rasmussen 2003; Markowski et al. 2003; Thompson et al. 2003, 2007). Radar characteristics of supercells are also generally well-known and have been used extensively in understanding in-storm processes, especially those that lead to tornadogenesis or tornadogenesis failure. These attributes are characterized by polarimetric radar variables that include reflectivity (Z_H), differential reflectivity (Z_{DR}), copolar cross-correlation coefficient (ρ_{hv}), and radial velocity (V_R). However, the usefulness of these fields depends on the temporal and spatial resolution of the radar and its ability to resolve processes that occur on short temporal and / or spatial scales.

The understanding of supercell and tornado dynamics has been greatly supplemented by the proliferation of higher spatiotemporal resolution data, especially from rapid-scan, polarimetric mobile radars (Bluestein et al. 2004; Alexander and Wurman

2005; Bluestein et al. 2007a,b; Kosiba and Wurman 2010; Wurman et al. 2012, 2013; Wurman and Kosiba 2013). Finescale processes within supercells and tornadoes can evolve on timescales as short as $\sim$1 – 10 s, orders of magnitude smaller than the volume update time of the Weather Surveillance Radar 1988 Doppler (WSR-88D) radars. For example, high-resolution polarimetric data have allowed for the ability to document evolution of tornado debris signatures (TDSs; Ryzhkov et al. 2005b; Bluestein et al. 2007a; Kumjian and Ryzhkov 2008; Palmer et al. 2011; Bodine et al. 2013; Snyder and Bluestein 2014), characterized by high Z_H, low Z_{DR}, and low ρ_{hv} collocated with a tornado vortex signature (TVS; Ryzhkov et al. 2005b), including finescale debris ejections that occur in conjunction with rear-flank downdraft (RFD) surges (Houser 2013; Knox et al. 2013; Houser et al. 2015; Kurdzo et al. 2015). While studies have thoroughly documented RFD surges using in-situ observations (Markowski 2002; Grzych et al. 2007; Hirth et al. 2008; Lee et al. 2012; Atkins et al. 2014; Skinner et al. 2014), and have attempted to relate RFD characteristics to mesocyclone evolution (Adlerman et al. 1999; Finley and Lee 2004; Adlerman and Droegemeier 2005; Skinner et al. 2014), studies documenting RFD surges through high-temporal polarimetric radars are relatively scarce.

Storm inflow and directional shear within the supercell environment influences the spatial distribution of hydrometeors, which results in distinct low-level polarimetric signatures. The Z_{DR} arc is a band of relatively high Z_{DR} located along the leading edge of the forward-flank downdraft (FFD) as a result of drop size sorting (Kumjian and Ryzhkov 2008; Kumjian et al. 2010). Palmer et al. (2011); Crowe et al. (2012)

suggested that increased organization of the Z_{DR} arc, marked by an increase in curvature and magnitude (maximum Z_{DR} values), can be indicative of increasing likelihood of tornadogenesis. Similarly, Romine et al. (2008) identified a band of relatively high values of K_{DP} defined as the K_{DP} foot, located in the center of the forward-flank precipitation core where liquid water content is relatively high. Increasing areal extent of the K_{DP} foot and shifting of the location to downshear of the updraft can also allude increased tornadogenesis likelihood (Crowe et al. 2012; Loeffler and Kumjian 2018). Loeffler and Kumjian (2018) analyzed both the Z_{DR} arc and K_{DP} foot in quasi-linear convective systems and concluded that the relative location between them can yield information on preferred times of tornadogenesis, and that the angle between the two can be used to infer trends of storm-relative helicity (SRH).

Strong vertical velocities within the supercell updraft also results in identifiable polarimetric signatures above the 0°C level. Within the updraft, perturbation of the 0°C level upward by strong upward motion and delayed freezing of liquid hydrometeors results in higher concentrations of supercooled droplets at a particular elevation. Since liquid droplets are associated with larger Z_{DR} values relative to ice crystals, the result is a small region of higher Z_{DR} centered on the updraft, known as the Z_{DR} column (Hall et al. 1984; Illingworth and Caylor 1988; Conway and Zrnić 1993; Brandes et al. 1995). Similarly, the K_{DP} column, located adjacent to the Z_{DR} column, is thought to be the result of shedding of water droplets from wet hailstone growth and / or an abundance of mixed-phase hydrometeors, both of which leads to high water content above the 0°C level (Hubbert et al. 1998; Loney et al. 2002). Thus, Z_{DR} and

K_{DP} column have been used to infer updraft characteristics, with deeper columns associated with stronger updrafts (Picca et al. 2015; Dalman et al. 2018)

Another method to study microphysical characteristics of supercells is the use of the hydrometeor classification algorithm (HCA) to discern hydrometeor types based on Z_H, Z_{DR}, ρ_{hv}, and K_{DP}. Many studies implement a fuzzy logic classification scheme (Liu and Chandrasekar 1998; Vivekanandan et al. 1999; Liu and Chandrasekar 2000; Zrnić et al. 2001; Dolan and Rutledge 2009) which utilize weight and membership functions to assign classes. Typical classifications include ground clutter, ice crystals, snow, rain, hail, and a combination of classes such as a mixture of rain and hail. However, the HCA is adaptable to include other distinct polarimetric signatures, e.g., the addition of a TDS class in tornadic cases (Snyder and Bluestein 2014).

On 20 May 2013, a long-track EF-5 tornado tracked through the south side of the Oklahoma City metro, impacting Newcastle and Moore, Oklahoma and leaving behind extensive damage (Atkins et al. 2014; Ortega et al. 2014; Kurdzo et al. 2015). The supercell tracked within the observable region of a suite of polarimetric radars — among which was the PX-1000 radar, a transportable rapid-scan polarimetric X-band radar — and thus is well-suited for documentation of finescale processes and polarimetric features discussed previously (Cheong et al. 2013). The PX-1000 was positioned among several radars including three WSR-88D S-band Doppler radars that established a multiple-Doppler coverage of the Oklahoma City metro. This network of radars consists of mainly experimental and operational WSR-88Ds: 1) Twin Lakes, Oklahoma (KTLX), 2) Norman, Oklahoma (KOUN), and 3) Norman, Oklahoma (KCRI). The combination of 20-s single elevation plan position indicators

(PPIs) from PX-1000 and nearby volumetric data from KTLX, KOUN, and KCRI allows for the opportunity to assess finescale evolution of the supercell and tornado using PX-1000 along with vertical structure of the supercell using WSR-88Ds. While previous studies have analyzed data from 20 May 2013 during the mature stage of the supercell (Atkins et al. 2014), including one study using PX-1000 data (Kurdzo et al. 2015), the objective of the present study is to analyze dual-polarization signatures that detail storm-scale processes between (i) the early evolution of the supercell through tornadogenesis — ∼1930 to 1956 UTC — and (ii) from tornadogenesis through tornado intensification — ∼1956 to 2008 UTC.

While the inference of storm-scale processes through polarimetric radar data has been well-documented, studies investigating the correlation between various signatures and its implications to mesocyclogenesis / tornadogenesis, especially at high spatiotemporal resolution, is scarce. For this reason, RFD characteristics have been studied through in-situ measurements and there is a general lack of studies detailing polarimetric RFD evolution at high-temporal resolution. Furthermore, though the Z_{DR} arc has been studied quite extensively, less attention has been paid to characteristics and evolution of the K_{DP} foot. Analysis of the Z_{DR} arc and K_{DP} foot is also generally restricted to a single elevation — volumetric analysis of these features have yet to be conducted. Furthermore, studies citing behavior of the Z_{DR} arc in relation to the K_{DP} foot and similarly, Z_{DR} column to K_{DP} column, are uncommon, with supplementation of this analysis with rapid updates even more so. The purpose of this study aims to address:

1. documentation of finescale evolution within the supercell and hook echo using high-temporal, polarimetric PX-1000 data,

2. evolution of RFD surges and associated polarimetric signatures, including the detection of pre-tornadogenesis tornadic debris signatures (pTDSs), and

3. evolution of Z_{DR} and K_{DP} signatures leading up to and during tornadogenesis, and its relation to storm-scale processes including drop size sorting and updraft characteristics.

Chapter 2 provides a background of radars and polarimetric variables as well as supercell dynamics and structure. Chapter 3 outlines the data and methods used within the analysis. An event overview and discussion of key findings are presented in Chapters 4 and 5, with conclusions and recommendations for future work provided in Chapter 6.

Chapter 2

Background

Since the 1940s, radars have been used as a tool to remotely observe the atmosphere in real-time through electromagnetic wave scattering. The applications of radars has greatly expanded with the advancement of technology and the necessity to improve meteorologically, both in terms of operation and research. The applications of radars are broad, from precipitation detection and quantitative precipitation estimates (QPE) (Maynard 1945; Marshall and Palmer 1948) to distinguishing size, shape, and concentration of hydrometeors (Kumjian and Ryzhkov 2008), made possible by the implementation on dual-polarization to the WSR-88D radars.

Table 2.1: Categories of weather radar bands and their corresponding wavelength.

Band	Wavelength (cm)
K	0.75 – 2.5
X	2.5 – 4
C	4 – 8
S	8 – 15

Weather radars typically operate with a wavelength between 0.1 cm to 15 cm, and within this range there are several different categories or "bands" according to the wavelength (Table 2.1). While longer wavelength radars are more expensive since they require a larger antenna for the same angular resolution, and thus they must remain on a fixed-site, they are less subject to attenuation. For example, the WSR-88D

radars operate at 10-cm wavelength (S-band). On the other hand, attenuation for K- and X-band radars can be problematic. However, the reduced antenna size makes shorter-wavelength radars ideal for transport. Additionally, smaller, lighter antennas allow the radar to achieve a faster rotation rate providing higher spatiotemporal resolution data, making them suitable for mobile research radars such RaXPoL and the PX-1000 (Pazmany et al. 2013; Kurdzo et al. 2015). While K-band radars can provide the highest resolution data, the attenuation of these radars are so significant that their use for studies of convection is much more limited compared to X-band radars.

As stated previously, radars operate on the properties of electromagnetic wave scattering by emitting discrete electromagnetic pulses. The time in between two subsequent pulses is known as the pulse repetition time (PRT; T_s), and determines the maximum range and radial velocity that the radar can measure without ambiguity. The maximum unambiguous range is given by

$$r_a = \frac{cT_s}{2} \tag{2.1}$$

where $c = 3 \times 10^8$ m s^{-1} is the speed of light. The factor of 2 in the denominator is necessary to take into account that the beam has to travel to the location of the scatterers and back (two-way path). It is possible that scatterers beyond this maximum unambiguous range create echoes detectable by the radar, but the radar will have sent out another pulse by this time. Therefore, the radar will infer that the echo has come from its most recent pulse, putting the scatterer much closer than

in reality. This is referred to as second-trip echoes or range folding and usually is detectable because the storm that is beyond r_a appears elongated and unrealistic. The PRT also governs the maximum unambiguous velocity, given by

$$v_a = \pm \frac{\lambda}{4T_s} \tag{2.2}$$

where λ is the wavelength of the radar. If a target is moving faster than v_a, the phase shift will be such that the PRT cannot adequately sample the phase and therefore the velocity will "wrap around" (alias) and be erroneously reported. For the same PRT, higher wavelength radars, e.g., 10-cm S-band radars such as the WSR-88D, have a higher v_a compared to shorter wavelength radars such as X-band or C-band radars. Combining Equations (2.1) and (2.2) by solving for T_s, we end up with the equation

$$v_a r_a = \frac{c\lambda}{8} \tag{2.3}$$

where the RHS of the equation is a constant for a given radar. This means that if one wants to increase the unambiguous velocity, the unambiguous range will decrease and vice versa. This is known as the Doppler Dilemma. An appropriate PRT must be chosen such that there is a good balance between r_a and v_a depending on the situation.

Once the radar sends out a pulse, it switches into listening mode for returned echoes. The power returned by a point target is given by the radar equation for point targets,

$$P_r = \frac{P_t g^2 \lambda^2 \sigma_b f^4(\theta, \phi)}{(4\pi)^3 r^4 l^2} \tag{2.4}$$

where P_t is the power transmitted, g is the gain of the antenna, σ_b is the backscatter radar cross section, r is the range to the target, and l is the losses due to attenuation. $f^4(\theta, \phi)$ has a value ranging from 0 to 1 and has to do with the illumination pattern of the beam and where the target is in relation to the center of the beam. If the target is exactly in the center of the beam, then $f(\theta, \phi)^4 = 1$. Notice that r in the denominator is to the 4^{th} power, and therefore the returned power decreases drastically as the target gets farther away from the radar. However, for weather radar applications, it is never the case where a single point target must be measured by the radar. Rather, is it much more useful to measure a volume of scatterers. This is introduced by the weather radar equation, which is similar to Equation (2.4) but has important differences. Mathematically, it is written as

$$P_r = \frac{P_t g^2 \eta c \tau \pi \theta^2 \lambda^2}{(4\pi)^3 r^2 l^2 16 ln(2)} \tag{2.5}$$

where θ is the half-power beamwidth in radians and τ is the pulse length. For a spherical water droplet, η is given by

$$\eta = \frac{\pi^5}{\lambda^4} |K_w|^2 \int_0^\infty D^6 N(D) dD, \tag{2.6}$$

where $|K_w|^2$ is the dielectric constant for liquid water ≈ 0.92, D is the diameter of the drop and $N(D)$ is the number of drops per unit volume per unit diameter. One of the most important distinctions between Equation (2.4) and (2.5) is that for the radar equation, the r on the bottom to the second power rather than to the fourth. Therefore, the loss in power with range is not as significant when expressing the radar equation in terms of distributed scatterers such as raindrops.

Both radar equations take into account the backscatter cross section of the targets σ_b, which depends on both the orientation of the target in relation to the radar as well as its size relative to the wavelength of the radar. In terms of the size, there are three main regimes (Figure 2.1) that change the equation of σ_b. For a spherical raindrop with diameter D, if $D > \lambda$, then the raindrop is considered to be in the optical regime and

$$\phi_b \approx \frac{\pi D^2}{4} \tag{2.7}$$

which means σ_b is dependent on the size of the drop. If $D \leq \lambda/16$, then the drop is in the Rayleigh regime and

$$\phi_b = \left(\frac{\pi^5}{\lambda^4}\right)|K_w|^2 D^6 \tag{2.8}$$

. The Rayleigh regime is the most common regime for raindrops. Notice that σ_b is again dependent on the size of the scatterer. However, for $D \sim \lambda$, the drops are in the Mie regime and relating the power returned to the size becomes much more complicated, since the EM wave wraps around the hydrometeor and may interact constructively or destructively to the return wave. In such cases, σ_b does not have a monotonic trend with diameter.

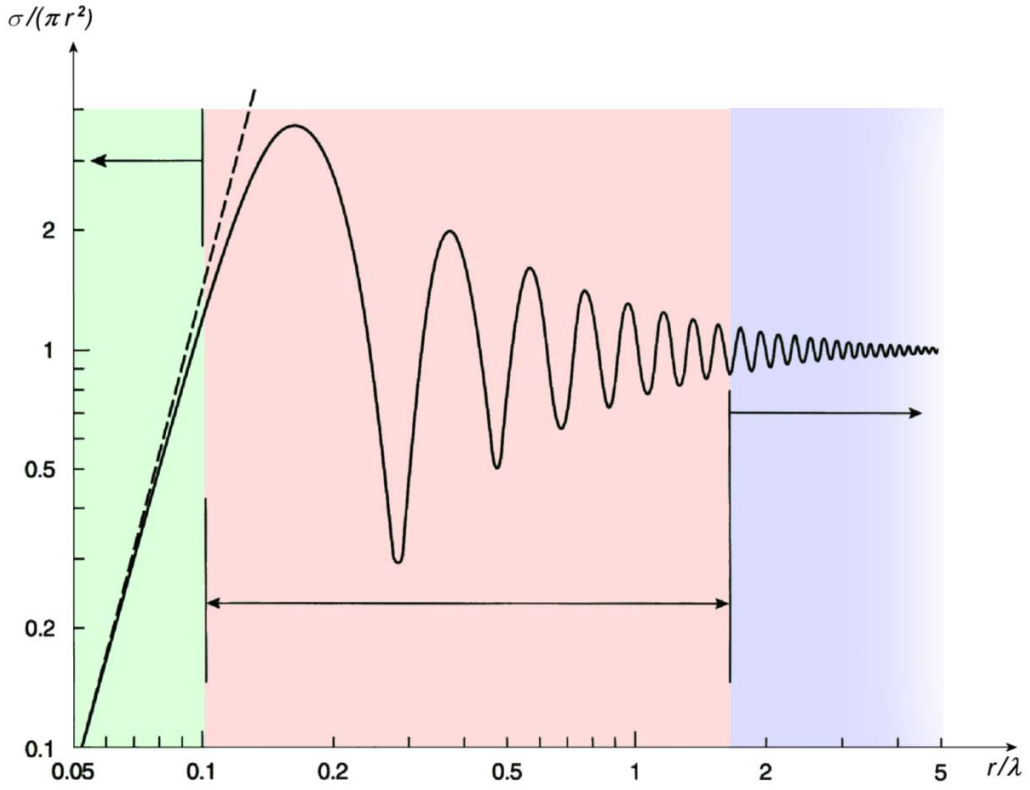

Figure 2.1: Radar cross-section of a sphere in the Rayleigh (green), Mie (red), and optical regimes. Graphic courtesy of Wolff (1998).

2.1 Polarimetric Variables

Similar to single-polarization radars, dual-polarization radars measure three moments - Z_H, V_R, and Doppler spectrum width (W) - but in both the horizontal and vertical polarizations. The additional measurements of backscatter in both polarizations provides measurements of Z_H, Z_V, V_H, V_V, W_H, and W_V. With the use of amplitudes and phases of returned echoes, additional variables can be calculated providing information about the characteristics of the scatterers such as type, shape, size, concentration, and orientation. These variables include Z_{DR}, differential propagation phase shift (ϕ_{DP}), K_{DP}, and ρ_{hv}. Physical interpretations of each of these variables will be discussed in context of supercells below.

2.1.1 Radar Reflectivity Factor

The most fundamental use of radars is the ability to detect areas of precipitation, typically displayed as reflectivity factor, Z. For a particular volume, Z is dependent on both the concentration of scatterers as well as the size distribution. Mathematically, it is expressed as

$$Z = \int_0^\infty N(D) D^6 dD. \tag{2.9}$$

Z is most often measured on a logarithmic scale in units of decibels of Z, or dBZ, given by

$$Z_{dBZ} = 10 log_{10}\Big(\frac{Z}{Z_0}\Big) \tag{2.10}$$

where Z_0 is the return from a 1 mm drop in a 1 m^3 volume. Because Z is a variable that relies on the returned power, it is affected by attenuation and therefore must be used with caution when analyzing areas of heavy precipitation. This is especially problematic for radars with shorter wavelengths, such as X-band radars, as attenuation problems are magnified.

For liquid precipitation, as the number of drops increases or average drop size increases, Z also increases. Because Z is a function of D^6 (when Rayleigh scattering is valid), if a sampling volume has both small raindrops and large raindrops, the return signal will be dominated by the larger raindrops rather than the small raindrops. Though refractive index of ice is lower than that of water, hailstones will exhibit larger values of Z merely due to their size in relation to nearby raindrops. For melting hail coated with a torus of water, the radar will perceive this as larger raindrops and Z will be relatively large.

For non-meteorological targets, the behavior of Z can range drastically depending on the scatting mechanism. Radar can often capture large flocks of birds and bats, and can even capture smaller biological targets such as insects if the concentration is high enough (Lakshmanan et al. 2010; Chilson et al. 2012). Besides biological scatterers, radars are also useful in detecting tornadic debris (Bodine et al. 2014; Van Den Broeke and Jauernic 2014; Griffin et al. 2017). The presence of lofted debris particles (e.g., dirt, leaves, structural fragments) are associated with high Z due to their large size relative to adjacent raindrops. This signature is known as the "debris ball". Radar can also capture objects that are stationary relative to the ground such as buildings, wind turbines, or even the ground itself when the radar beams bends back towards

the surface, known as anomalous propagation. The resulting Z (hereafter, Z_H) tends to be greater as these targets are typically larger than meteorological scatterers.

2.1.2 Differential Reflectivity Factor

Differential reflectivity, defined as

$$Z_{DR} = 10 \log_{10} \left(\frac{Z_H}{Z_V} \right), \tag{2.11}$$

is a measure of the reflectivity-weighted axis ratio of the target given in units of decibels, or dB (Seliga and Bringi 1976). Targets with high Z_{DR} indicate that Z_H is greater than Z_V, and represent scatterers that are aligned in the horizontal. Likewise, targets with their major axis aligned in the horizontal vertical polarization produce positive Z_{DR} and targets that return equal power in both the horizontal and vertical polarizations produce a Z_{DR} of 0 dB. For liquid precipitation, smaller raindrops tend to be more spherical and have a lower Z_{DR} as opposed to large raindrops which are oblate and have a high Z_{DR}. The largest raindrops can have Z_{DR} values in excess of 7 dB.

Small hailstones tend to be spherical and therefore also have a Z_{DR} of around 0 dB. Though larger, especially giant, hail tends to have a spiky, irregular shape, these hailstones tumble while they fall and give the illusion of a spherical shape; thus, even large hailstones have a Z_{DR} close to 0 dB. Melting hailstones on the other hand can observe a variety of Z_{DR} values due to the presence of a torus of liquid water (Ryzhkov et al. 2013). The more liquid water, the larger the increase in Z_{DR}.

Moreover, larger hailstones have an easier time shedding the torus of water. Therefore, a small melting hailstone having a largely positive Z_{DR} in contrast to a large melting hailstone which would have a small positive Z_{DR}.

Similar to Z_H, Z_{DR} tends to be much more variable for non-meteorological targets. Biological scatterers such as birds and insects are typically associated with a high Z_{DR} since biological scatterers tend to have elongated bodies oriented in the horizontal. However, in terms of other non-meteorological scatterers, Z_{DR} can range depending on the type of scatterer and the degree of alignment between those scatterers. For example, smoke and ground clutter can vary widely in Z_{DR}, but typically exhibit positive or negative Z_{DR} values exceeding those of hydrometeors. Tornadic debris on other hand proves to be much more complicated. Though it is an open question, observational research has found that tornadic debris tends to observe either near zero or negative Z_{DR} (Bodine et al. 2013; Van Den Broeke and Jauernic 2014). The leading theory suggests that despite the irregularity of tornadic debris, and random tumbling, there tends to be a vertical degree of alignment, especially in smaller debris particles such as leaves and blades of grass (Umeyama et al. 2018). However, non-Rayleigh scatterers cannot be dismissed as such scatterers would negatively bias the measurement.

2.1.3 Differential Propagation Phase Shift and Specific Differential Phase

The EM waves that are emitted in the horizontal and vertical polarizations are inherently affected by scatterers through propagation and phase shifts. If the pulse travels through clear air, the horizontal and vertical waves travel at the same speed and there is no difference in their phase. However, once the EM pulse passes through a scatterer, such as a raindrop, the pulse is slowed due to its high refractive index. If the a scatterer is spherical, the pulse is affected in both the horizontal and vertical directions equally and there is again no difference in the horizontal and vertical phases after passing through the raindrop. However, if the raindrop is oblate, the horizontal pulse will be slowed down more than the vertical pulse, and therefore the horizontal phase lags behind the vertical phase by a certain degree. This is known as the differential propagation phase shift, or ϕ_{DP}. If the horizontal pulse lags behind the vertical pulse, then ϕ_{DP} greater than 0, and vice versa. As the scatterer size in a volume increases, ϕ_{DP} also tends to increase. ϕ_{DP} is also proportional to the concentration of scatterers within the volume since more interactions with rain drops increases the overall phase shift.

One advantage to using ϕ_{DP} is that since it is a phase measurement, it is not affected by attenuation, partial beam blockage, calibration of the radar, among power-based measurements like Z_H and Z_{DR}. Therefore, one of the most important applications for ϕ_{DP} is its usefulness in attenuation correction as well as its capability of

providing QPE. However, ϕ_{DP} is not an intuitive variable. Thus, K_{DP}, which is the rate at which ϕ_{DP} changes, is often used to interpret the phase shift in the range.

For liquid precipitation, K_{DP} will be highest where areas of liquid water content are the highest. Thus, while Z_H and Z_{DR} tend to be largest where raindrops are largest, K_{DP} is largest where there are a large number of small or medium sized raindrops. Because K_{DP} is directly related to water content within a volume, K_{DP} can be a useful variable for QPE. In fact, the relationship between K_{DP} and rainfall rate has been shown to be nearly linear (Sachidananda and Zrnić 1987) and can even be used to estimate lighter precipitation over the long-term where K_{DP} can be quite noisy. While K_{DP} is not affected by tumbling hail due to the "spherical" shape, regions of mixed-phase precipitation such as wet hail can also have large K_{DP} values.

Unfortunately, K_{DP} can be difficult to decipher for non-meteorological targets. The first problem is that some non-meteorological targets such as birds are large enough to be seen as non-Rayleigh scatterers by the radar. In such cases, a backscatter phase shift is produced by these targets and may result in large positive or negative values. The same issue occurs with large hail. In other cases, non-meteorological scatterers can vary wildly in shape and size, such as with tornado debris. Due to this, copolar cross-correlation coefficient values can be low. The increased variability of the scatterers makes it nearly impossible to obtain reliable estimates of K_{DP}. Therefore, operationally, K_{DP} is usually only calculated for areas exceeding a certain correlation coefficient.

2.1.4 Copolar Cross-Correlation Coefficient

ρ_{hv} is an indication of the diversity of scatters in a sampling volume as measured by the co-polar correlation between the returned signals in the horizontal and vertical polarizations. In other words, ρ_{hv} measures the similarity of scattered horizontal and vertical pulses. These signals provide information about the physical characteristics of the volume of scatterers, including type, shape, and orientation. Thus, for a volume of scatterers consisting of a variety of scatterers (e.g., a mixture of hail and rain) ρ_{hv} would be low. On the other hand, more uniform scatterers within a sampling volume would lead to a high ρ_{hv} value (i.e., closer to 1). An advantage of ρ_{hv} is that it is not dependent on particle concentration and/or size and is also resistant to attenuation, beam blockage, and miscalibration of the radar.

For pure rain, the scatterers within the sampling volume are nearly identical to one another since the size and shape of the raindrops do not change drastically within the volume. Therefore, ρ_{hv} tends to be high (> 0.95). However, due to the oblateness of large raindrops and also effects from slight wobbling as they fall, ρ_{hv} will be slightly lower in value than with smaller, more spherical raindrops which will produce values closer to 1. Sampling volumes consisting of hail will tend to produce lower values of ρ_{hv} due to their large sizes and associated Mie scattering. However, there are some exceptions to this. Regions of wet hail can produce even lower ρ_{hv} values due to the mixture of water and ice. Secondly, extremely large hail can also produce low values of ρ_{hv} due to their irregular, spiky shape.

Another important application of ρ_{hv} is the capability of distinguishing between meteorological and non-meteorological scatterers. In general, non-meteorological scatterers tend to produce low ρ_{hv} since they tend to be larger scatterers, more irregularly shaped than hydrometeors, and sometimes have higher refractive indices. Typical examples of non-meteorological scatterers include biological scatterers (e.g., birds, bats, insects), man-made scatterers (e.g., buildings, turbines), and inorganic scatterers (e.g., smoke, dust). ρ_{hv} is especially useful for detecting debris that may be lofted by tornadoes. This signature is commonly referred to as a TDS and has been noted in many studies of polarimetric observations of severe thunderstorms (e.g., Ryzhkov et al. 2005a).

2.1.5 Radial Velocity

V_R a measure of the velocity towards or away from the radar, i.e., the radial component. Although the radar measures both V_H and V_V, only the former is typically used for velocity measurements and thus V_H and V_R are interchangeable. The radar measures V_R as a rate of change of the difference in returned phase shift compared to the emitted beam. Because the radar only measures the radial component, any velocities moving parallel to the radar will be zero. In the context of supercells, V_R is useful in identifying areas of inflow and outflow, such as strong wind gusts within the rear flank downdraft. Additionally, V_R makes the detection of tornadoes with radars possible. In particular, strong, compact rotation in the low-levels, i.e., a couplet, indicates the presence of a low-level mesocyclone and can be used as an indicator for a developing or occurring tornado, known as a TVS.

2.2 Supercells

2.2.1 Environmental Characteristics

Environmental conditions have a profound influence on convective storm modes. Factors such as instability, wind shear, moisture and forcing/lift are among the leading contributors to determine storm mode(s). Slight modifications of the environment (small- or large-scale) can drastically alter forecasts and be the difference between a cluster of thunderstorms or discrete supercells. Each of the different storm modes are capable of producing various hazards but vary in degrees of severity. One of the most notorious of the storm modes are supercells because of its overall strength and intensity, as well as life-threatening impacts. Typical hazards for supercells include damaging winds, large hail, torrential rain, and occasionally tornadoes. The organization, maintenance, and severity of a supercell are dependent on the deep, persistent mesocyclone. There are three classifications of supercells: classic, high-precipitation (HP), and low-precipitation (LP), each of which are dependent on environmental conditions, as well as two terminologies describing the evolution of supercells: cyclic and non-cyclic (Lemon and Doswell 1979; Weisman and Klemp 1982).

The environment favorable for supercell development relies on several factors. Supercells in particular are susceptible to variations in environmental wind shear, both in magnitude and direction. Firstly, the deep layer wind shear vectors should be near-perpendicular to the boundary; otherwise, conditions are not favorable for maintaining discrete convection and favor a multicellular mode. Secondly, the vertical wind field should veer with height which promotes dominant right-moving supercells

and its magnitude should be on the order of 35-40 kts or greater. Additionally, for tornadic supercells, strong low-level (0-1 km) wind shear is beneficial, typically on the order of 15-20 kts or greater. Supercells also require decent instability for explosive growth usually denoted by mixed-layer convective available potential energy (ML-CAPE) greater than 1000 J kg^{-1}. However, tornadoes have occurred in lower CAPE environments as a result of strong vertical wind shear. High CAPE environments are supported by steep mid-level lapse rates, ample moisture, and relatively low dewpoint depressions. In order for supercells to initiate, there must be strong forcing usually provided by a boundary such as a cold front or dryline. There also must be relatively low convective inhibition (CIN) which can be eroded by an increase in moisture and temperature and broad synoptic-scale lift.

2.2.2 Structure and Dynamics

Figure 2.2 shows a diagram of an idealized supercell with the locations of the RFD, FFD, updraft, and gust front with associated streamlines. Warm, moist air is drawn into the updraft and is denoted by a notch in the gust front. The FFD is typically located to the northeast of the updraft and usually contains the heaviest precipitation region. As the mesocyclone matures, some of the precipitation from the FFD is cyclonically wrapped around the updraft and descends to the southwest of the updraft, resulting in the RFD. The cyclonic wrapping of precipitation is what gives the supercell its classic kidney bean shape when viewed on radar. Not only can the RFD contain extremely strong winds, but its characteristics have been found to be important for tornadogenesis mechanisms (Lee et al. 2012; Skinner et al. 2014; Mashiko

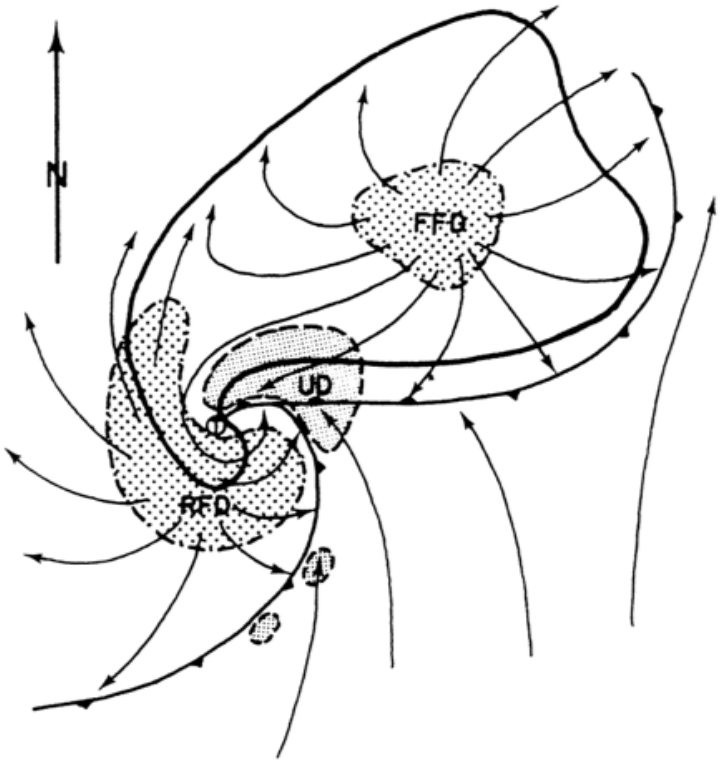

Figure 2.2: Schematic of supercell structure showing the location of the updraft (UD), FFD, and RFD. Graphic courtesy of Markowski (2002).

2016). Note that in HP supercells the precipitation in the RFD may wrap completely around the updraft while in LP supercells the RFD may not have any precipitation. In an ideal case, the gust front would remain relatively close to the precipitation cores; if the gust front surges too far ahead of the precipitation, the warm, moist air feeding the updraft may be cut off.

The FFD is the result of the descent of rain-cooled air. This descent is due to both evaporation and melting of hail as well as precipitation loading. As the forward flank gust front propagates, warm, moist air is lifted which helps to maintain precipitation in the FFD. Additionally, the temperature contrasts between the warm inflow and the cool air within the FFD baroclinically-induced low-level horizontal

vorticity along the boundary. In fact, magnitude of baroclinic vorticity can match or be greater than environmental vorticity (at least in simulations). The updraft then tilts the low-level baroclinic horizontal vorticity which produces significant low-level vertical vorticity and enhances mid-level vertical vorticity. However, this is still not a sufficient condition for the formation of tornadoes since tilting cannot produce vertical vorticity at the surface. Thus, tornadoes may rely on a downdraft to bring vorticity to the ground, a possible role of the RFD.

Though there have been many studies done on understanding the role of the RFD, the complex role of this region in tornadogenesis remains poorly understood (Markowski 2002; Markowski and Richardson 2009). The presence of the RFD is due to the combination of thermodynamic and dynamic effects. Thermodynamically, evaporative cooling from cyclonically wrapping precipitation leads to negative buoyancy and descending air. Dynamically, the updraft acts as a solid column which blocks upper-level flow leading to a downward-oriented vertical pressure gradient force that forces air to descend. If the dynamic processes outweigh the effects of thermodynamic processes in the maintenance of the RFD, the RFD winds at the surface may actually be warmer than its surroundings due to warming during adiabatic descent. The thermodynamic properties of the RFD winds near the surface can have a significant impact on tornadogenesis (Markowski 2002; Grzych et al. 2007). If the RFD winds are able to wrap back around the updraft near the surface and the air is sufficiently buoyant, the stretching of near surface vorticity may occur, a precursor to tornadogenesis.

The updraft is a region of little to no precipitation as a result of high vertical velocities, excluding some HP supercell cases. On radar, the updraft is discernible at upper-levels by a bounded weak echo region (BWER) due to the lack of precipitation. The rotating updraft in supercells typically maintains vertical vorticity on the order of 10^2 s^{-1} for a sufficient period of time. The vertical vorticity in the mid-levels is generated by the tilting of streamwise, horizontal vorticity created by the ambient wind shear. Once the updraft intensifies, stretching also plays an important role in the maintenance of vertical vorticity. At early stages in the updraft life cycle, there are two terms that govern the behavior of the updraft: the linear and nonlinear forcing terms. When the ambient wind shear lacks directional variation, the nonlinear dynamic forcing term dominates which leads to stacked high and low pressures. Thus, in this case, the updraft does not favor one propagation direction over another, leading to a supercell split of a right and left-mover. When there is significant directional shear, the linear dynamic forcing term dominates and the high and low pressure centers align in such a manner that rightward propagation of the updraft is favored, which results in a so-called right-moving supercell.

Supercells often have more than one mesocyclone throughout its lifetime (sometimes simultaneously). The repeated generation of new mesocyclones is called cyclic mesocyclogenesis. This process is the result of the interactions between the updraft and the surging RFD. When the RFD and associated gust front surge outwards, the original mid-level mesocyclone occludes and strengthens due to tilting of the baroclinically generated horizontal vorticity and stretching of streamwise vertical vorticity from descending RFD air. Simultaneously, the surging gust front forces development

of a new updraft downshear, resulting in a two-celled updraft structure. As the gust front progresses, the downshear updraft continues to propagate further downshear while the warm air inflow into the original updraft is undercut. Thus, the new updraft replaces the original mesocyclone. The process of cyclic mesocyclogenesis can repeat as long as the RFD continues to surge and occlude the mesocyclone.

Chapter 3

Data and Methods

3.1 Radar Specifications

The analysis of the 20 May 2013 Moore, Oklahoma supercell utilizes four radar systems that were operating in and around the Oklahoma City metropolitan area and captured the entirety of the supercell's life cycle. Namely, the supercell was observed by three operational and experimental WSR-88Ds — KTLX, KOUN, and KCRI — and the University of Oklahoma Advanced Radar Research Center's PX-1000, a transportable, polarimetric, X-band radar. Table 3.1 lists analysis specifications for each of the radars operating on 20 May 2013. All WSR-88Ds radars had an azimuthal and range resolution of 1° (except for the lowest three elevations which oversampled to 0.5°) and 250 m, respectively, but varied in volume coverage and temporal resolution. KTLX and KCRI collected data in a standard volume coverage pattern with 14 elevations (VCP 12) spanning from 0.5° to 19.5°, resulting in a volume update rate of ∼4-5 minutes. KOUN was however modified to operate in rapid-scan, sectorized scanning strategy as part of National Severe Storm Laboratory's (NSSL) Rapid-Scan Polarization Experiment (Burgess et al. 2014). The VCP for KOUN was more shallow compared to KTLX and KCRI, spanning only from 0.5° to 10°, but resulted in an update rate of ∼2-3 minutes.

Radar data collected from the PX-1000 has a range resolution of 112 m with an effective beamwidth (Doviak and Zrnić 1993) of 1.8°, oversampled to 30 m and 1°, respectively. The PX-1000 operates using a pulse compression scheme (Kurdzo et al. 2014) resulting in a sensitivity of approximately 20 dBZ at 50 km. To reconstruct the blind range, a time-frequency multiplexing (TFM; Cheong et al. 2013) method is implemented using a short pulse of 2 μs to obtain data within 10.3 km during the long-pulse transmission (so-called blind range). Though the resulting sensitivity is still marginally diminished, TFM sufficiently resolves robust echoes such as those associated with the supercell on 20 May 2013; thus, TFM does not affect the analysis since the supercell is outside the fill pulse region. In addition to the TFM, a multilag method was used (Lei et al. 2012) to increase the accuracy and transition across the blind range by reducing the susceptibility of ρ_{hv} to low signal-to-noise (SNR) areas. However, the multilag method is inadequate in regions of high spectrum width; instead, pulse-pair processing was used to process gates with lag-2 spectrum widths greater than 2 $\mathrm{m\,s^{-1}}$ and SNR greater than 10 dB.

As a result of the relatively shorter X-band wavelength of PX-1000 (3.14 cm), attenuation effects are magnified when compared to the other three radars which are S-band with a wavelength of at least 10 cm. Thus, attenuation correction for the PX-1000 must be implemented using the method described in Snyder et al. (2010) in order to avoid large errors for Z_H and Z_{DR} in regions of heavy precipitation. Attenuation correction is performed first by summing up the K_{DP} field over each range gate to get a cumulative differential phase, or ϕ_{sum}. In order to avoid corrections in areas where the beam is too close to the radar or where Z_H is low, the K_{DP} field is set to

0 for the first 30 range gates and for Z_H less than 30 dBZ. Additionally, in order to avoid negative attenuation corrections, anywhere the K_{DP} field is negative is also set to 0. ϕ_{sum} for each range gate is then multiplied by the linear coefficients, α (0.313) and β (0.0483), to compute the magnitude of attenuation correction for Z_H and Z_{DR}, respectively. Thus, the attenuation correction for each is mathematically given by

$$Z_{H_{corr}} = Z_H + \alpha\phi_{sum} \tag{3.1}$$

and

$$Z_{DR_{corr}} = Z_{DR} + \beta\phi_{sum} \tag{3.2}$$

For this analysis, data from all radars are linearly interpolated to a regular Cartesian grid with the exception of ΔV_{max}. PX-1000 is interpolated to a regular 0.1 $\times$ 0.1 km grid whereas KTLX, KOUN, and KCRI are interpolated to a regular 0.25 $\times$ 0.25 $\times$ 0.25 km grid. Additionally, data for each individual PPI scan within a full-volume scan for the WSR-88Ds were spatially corrected for storm motion to ensure vertical continuity, using 1) storm motion calculated from differences in the x and y center points — which are manually chosen at each time to represent the center of the low-level mesocyclone — and 2) time difference between the lowest elevation scan and that particular PPI. Afterwards, the data at each time were interpolated to the regular three-dimensional grid.

Table 3.1: Analysis specifications for PX-1000, KTLX, KOUN, and KCRI on 20 May 2013, consisting of the respective analysis periods and lowest beam height at the hook echo at the start of the analysis period (top), tornadogenesis (∼1956 UTC; middle), and end of the analysis period (bottom).

	PX-1000	KTLX	KOUN	KCRI
Analysis Period (UTC)	1930–2008	1929–2008	1947–2007	1949–2008
Beam Height (km)	1.1 0.74 0.59	0.35 0.24 0.20	0.16 0.14 0.12	0.19 0.14 0.11

3.2 Maximum ΔV

The strength of the mesocyclone was quantified by conducting a ΔV_{max} analysis for KOUN, KCRI, and PX-1000 as has been used a proxy in previous studies (French et al. 2013; Houser et al. 2015). Velocity dealiasing was performed manually using standard unfolding techniques via Solo II, a program developed by the National Center for Atmospheric Research, for each radar. Using the dealiased velocity, ΔV_{max} was then calculated by taking the difference between the maximum inbound and outbound velocities within a 2-km range of the center point. Data for ΔV_{max} were not interpolated to regular grids to avoid dampening of high velocities from interpolations.

3.3 Hydrometeor Classification Algorithm

The HCA was implemented to quantify the change in hydrometeors (and non-hydrometeors) within the supercell with time. Specifically, HCA will be important in quantifying the changes in heavy rain and hail and for this reason, the HCA separates hail into three categories: Small Hail (SH), Large Hail (LH), and Giant Hail (GH). Current methods for HCAs are mostly based on a fuzzy logic approach that involve membership

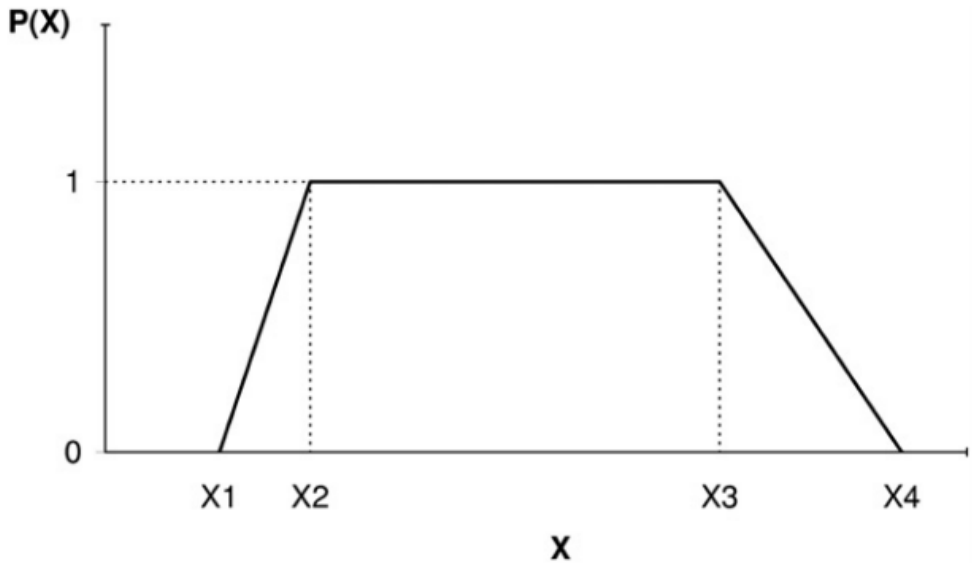

Figure 3.1: Membership function for a certain polarimetric value X, given by four increasing values X_1, X_2, X_3, and X_4.

functions and decision criteria. A method developed by NSSL (Schuur et al. 2003; Ryzhkov et al. 2005a; Park et al. 2009) specifically for WSR-88Ds will be utilized for this study which accounts for measurement error, beam broadening effects, melting layer, and precipitation type. This fuzzy logic approach consists of three steps - fuzzification, aggregation, and defuzzification. The fuzzification process defines a set of membership functions that differentiate between radar echo classes (e.g., rain, hail) based on polarimetric variables, namely, Z_H, Z_{DR}, and ρ_{hv}. The membership functions consist of four numbers which create a trapezoid for each polarimetric variables that distinctly represent each class (Figure 3.1). Any overlap in the membership functions depict areas of uncertainty, such as effects of Mie scattering. The aggregation then applies the membership functions to cost functions A_i which determine the

weight of the contribution and assigns a likelihood to the class. The defuzzification then chooses the class which has the highest overall value as the output class.

The Park et al. (2009) algorithm consists of ten classes: 1) Ground Clutter (GC) / Anomalous Propogation (AP), 2) Biological Scatterers (BS), 3) Dry Snow (DS), 4) Wet Snow (WS), 5) Crystals (CR), 6) Graupel (GR), 7) Big Drops (BD), 8) Rain (RA), 9) Heavy Rain (HR), and 10) Rain / Hail (RH). However, frozen precipitation (except hail) was excluded in this analysis to further restrict class categorization, especially for X-band, and instead further expands on RH to allow for the hail categorizations of SH (D <2.5 cm), LH (2.5< D <5 cm), GH (D >5 cm; adapted from Ryzhkov et al. 2013). The algorithm for X-band is further modified to reflect membership functions defined by Snyder and Ryzhkov (2015) that better represents Mie scattering regimes for X-band as compared to S-band. Note that the Z_H membership functions from Snyder and Ryzhkov (2015) are modified slightly for RA, HR, and RH to ensure that RA is representative of smaller drops (decrease in upper range of Z_H) and RH is more representative of hail-only points (increase in lower range of Z_H); modified values were compared against KTLX, KOUN, and KCRI to ensure consistency. Tables 3.2 and 3.3 lists the membership functions used for the HCA analysis in this study.

An additional modification was made to the HCA to include the classification of the TDS, enabling the quantification of the TDS that will supplement the observations in polarimetric fields. Membership functions for TDS are given in Tables 3.2 and 3.3 based on values from Snyder et al. (2010), with additional criteria consisting of ρ_{hv} less than 0.92 and Z_H greater than 25 dBZ. A radius restriction of less than 3 km

Table 3.2: S-band membership functions for Z_H, Z_{DR}, and ρ_{hv} for each of the HCA classifications as well as weights to determine the aggregation value. The functions are given in Appendix A.

	GC	BS	BD	RA	HR	RH	SH	LG	GH	TDS
					Z_H					
x_1	15	5	20	5	40	45	45	54	54	30
x_2	20	10	25	10	45	50	49	59	64	35
x_3	70	20	45	45	55	75	59	64	74	70
x_4	80	30	50	50	60	80	64	69	80	75
					Z_{DR}					
x_1	-4	0	f_{21}-0.3	f_{11}-0.3	f_{12}-0.3	-0.3	1	0.4	0	-2.5
x_2	-2	2	f_{22}	f_{13}	f_{14}	0	1.5	0.9	0.5	-1.5
x_3	1	10	f_{31}	f_{23}	f_{24}	f_{16}	2.5	1.9	1.5	1.5
x_4	2	12	f_{32}+1	f_{25}+0.5	f_{26}+0.5	f_{18}+0.5	4	3.5	2	2.5
					ρ_{hv}					.
x_1	0.5	0.3	0.92	0.95	0.92	0.85	0.94	0.88	0.8	0
x_2	0.6	0.5	0.95	0.97	0.95	0.9	0.96	0.92	0.88	0.01
x_3	0.9	0.8	1	1	1	1	0.98	0.98	0.96	0.85
x_4	0.95	0.83	1.01	1.01	1.01	1.01	0.99	0.99	0.98	0.92
					Weights					
Z_H	0.2	0.4	0.8	1	1	1	1	1	1	0.6
Z_{DR}	0.4	0.6	1	0.8	0.8	0.8	0.8	0.8	0.8	0.8
ρ_{hv}	1	1	0.6	0.6	0.6	0.6	0.6	0.6	0.6	1

was also applied to the criteria to prevent TDS detection far from the center of the low-level mesocyclone.

3.4 Z_{DR} and K_{DP} Detection

A significant portion of the analysis is focused on regions of enhanced Z_{DR} and K_{DP} at low-levels, Z_{DR} arc and K_{DP} foot, and at upper-levels, Z_{DR} and K_{DP} column. Analysis of Z_{DR} arc and K_{DP} foot gives insight on the evolution of low-level supercell

Table 3.3: As in Table 3.2, except for X-band. The functions are given in Appendix A.

	GC	BD	RA	HR	RH	SH	LG	GH	TDS
					Z_H				
x_1	15	24	5	40	45	45	54	54	30
x_2	20	29	10	47	55	49	59	64	35
x_3	70	49	37	57	65	59	64	74	70
x_4	80	54	42	62	75	64	69	80	75
					Z_{DR}				
x_1	-4	A_2-0.6	A_1-5	A_1-5	A_1-5	1	0.4	0	-2.5
x_2	-2	A_2-0.3	A_1	A_1	A_1	1.5	0.9	0.5	-1.5
x_3	1	A_3	A_2	A_2	A_2	2.5	1.9	1.5	1.5
x_4	2	A_2+1	A_2+0.5	A_2+0.5	A_2+0.5	4	3.5	2	2.5
					ρ_{hv}				
x_1	0.5	0.92	0.95	0.92	0.80	0.94	0.88	0.8	0
x_2	0.6	0.93	0.96	0.94	0.85	0.96	0.92	0.88	0.01
x_3	0.9	1	1	1	0.95	0.98	0.98	0.96	0.85
x_4	0.95	1.01	1.01	1.01	1.01	0.99	0.99	0.98	0.92
					Weights				
Z_H	0.2	0.8	1	1	1	1	1	1	0.6
Z_{DR}	0.4	1	0.8	0.8	0.8	0.8	0.8	0.8	0.8
ρ_{hv}	1	0.6	0.6	0.6	0.6	0.6	0.6	0.6	1

dynamics, while Z_{DR} and K_{DP} column provides information on updraft characteristics.

3.4.1 Z_{DR} Arc and K_{DP} Foot

Although the temporal resolution of PX-1000 far exceeds that of the WSR-88D, X-band wavelength makes the beam subject to attenuation. While the Z_{DR} arc is positioned along the leading edge of the FFD and is less likely to be affected by attenuation, the K_{DP} foot is located within the precipitation core of the FFD, upshear of the updraft, and is more likely to be attenuated. As a result of uncertainty with attenuation correction methods, the Z_{DR} arc and K_{DP} foot analysis will rely on KTLX and KOUN for consistency in interpreting results.

The analysis of the supercell is affected by multiple storm mergers throughout the period. To exclude the influence of the storm mergers on the Z_{DR} arc and K_{DP} foot analysis, a subjective mask was defined, consisting of an additional Z_H greater than 30 dBZ and ρ_{hv} greater than 0.85 restraint, such that only processes relating to the supercell were included. The additional Z_H and ρ_{hv} restraints are also used to eliminate noisy data and ensure precipitation-only processes.

While Z_{DR} arc and K_{DP} foot are relatively shallow features, restricted to below 2 km (Kumjian and Ryzhkov 2008, 2009), three-dimensional characteristics of these signatures are still important, with deeper areas representing consolidated regions. To assess the volumetric characteristics, a threshold is defined such that if a grid point has a value larger than the threshold, it is classified as an enhancement. The Z_{DR} and K_{DP} thresholds are 3.5 dB and 1.5 dB km^{-1}, respectively; these values are

consistent with thresholds used by Van Den Broeke (2016) and are constant through time for both radars.

For each horizontal grid point, the number of vertical grid points below 2 km for which Z_{DR} and K_{DP} are enhanced is multiplied by the vertical resolution (0.25 km) to get the depth field of the Z_{DR} arc and K_{DP} foot. The depth field is smoothed using a Gaussian Filter with a standard deviation of 0.5. From the depth field, the total volumetric extent of the Z_{DR} arc and K_{DP} foot is calculated by taking of the sum of the depth field multiplied by the horizontal area of each grid point (0.125 km^2). The 90^{th} percentile of the depth field is also calculated to quantify the deepest areas of the enhancement regions.

The position of the Z_{DR} arc in relation to the K_{DP} foot can be informative of low-level processes, including drop size sorting and tornadogenesis-likelihood (Loeffler and Kumjian 2018). The position at each time is given by the Z_{DR} and K_{DP} centroid, calculated as the mean x and y value of grid points in which the depth is greater than the 75^{th} percentile. The 75^{th} percentile isolates the locations in which the Z_{DR} and K_{DP} enhancement regions are most consolidated; else, diffuse / shallow regions of the Z_{DR} arc and K_{DP} foot may skew the location of the centroids. From the centroids, the separation distance and separation orientation are calculated based on methods from Loeffler and Kumjian (2018) (Figure 3.2). For each time, the separation distance is calculated by

$$d = \sqrt{(x_{Z_{DR}} - x_{K_{DP}})^2 + (y_{Z_{DR}} - y_{K_{DP}})^2} \tag{3.3}$$

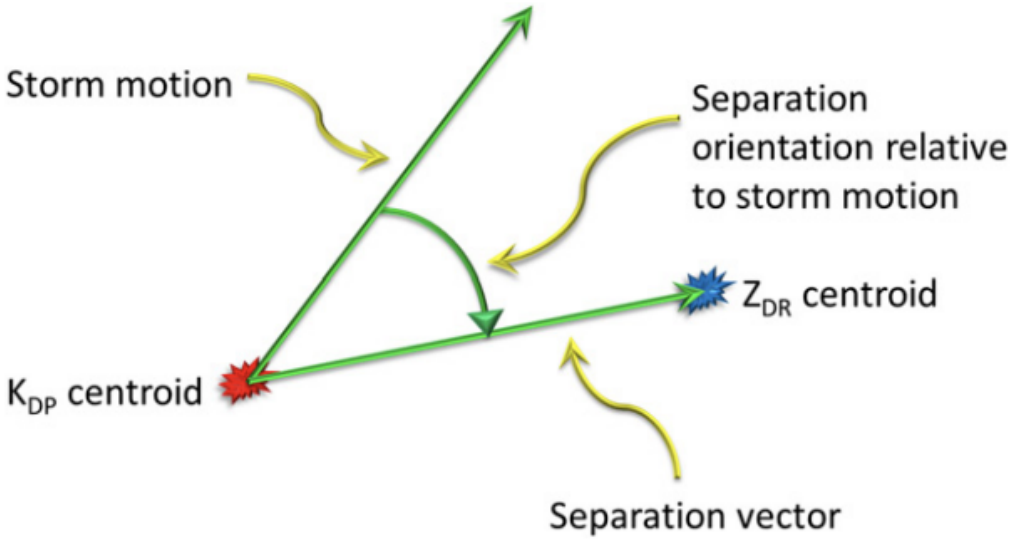

Figure 3.2: Schematic that shows the location of the K_{DP} centroid (red), Z_{DR} centroid (blue), the storm motion and separation vector, and the separation orientation which is the clockwise angle between the two vectors. Graphic courtesy of Loeffler and Kumjian (2018).

and the separation orientation is given as the clockwise-orientation angle between the storm motion vector and the separation vector. The storm motion vector connects the center points for the first and last scans in the analysis period while the separation vector connects the K_{DP} and Z_{DR} centroid at each time.

3.4.2 Z_{DR} and K_{DP} Column

The Z_{DR} and K_{DP} column analysis is conducted similar to the Z_{DR} arc and K_{DP} foot analysis. However, because these features should be collocated or in close proximity to the updraft, the data are restricted within 5 km of the center point. Additionally, since the Z_{DR} and K_{DP} columns exist above the 0°C level, only data above 4.2 km (based on the 1700 UTC sounding from Figure 4.1) are used. The depth

field is calculated using the same method as above, except for Z_{DR} and K_{DP} thresholds of 2.0 dB and 1.0 dB km^{-1}, respectively. The analysis proceeds similarly with calculations of volumetric extent, the 90^{th} percentile, the track of the centroid, and separation distance and orientation. However, because diffuse areas within the column are inherently eliminated through range restriction, the entire depth field is used for centroid calculations.

Chapter 4

High-Resolution Supercell and Hook Echo Analysis

4.1 Synoptic and Mesoscale Environment

At 1800 UTC, a 500 hPa positively-tilted trough extended over the western and central United States with an embedded 70-kt jet streak ejecting strong southwesterly upper-level flow into central Oklahoma. This was collocated with a south-southwesterly 30-kt low-level jet at 850 hPa which advected a deep moist layer from the surface up to 800 hPa. At the surface, a strong cyclone was situated over the North Dakota / South Dakota / Minnesota area associated with a cold front that extended down into southern Kansas and northwestern Oklahoma. This cold front intercepted a sharp north-south oriented dryline in western Oklahoma that pushed eastward through the late morning and afternoon hours. By 1600 UTC, a clear eastward bulge was evident in the dryline in southwestern Oklahoma that became the focus for convective initiation a few hours later.

Ahead of surface boundaries in the warm sector, southerly flow resulted in dewpoints greater than 21°C and surface temperatures between 26 – 29°C for central and eastern Oklahoma. Winds to the west of the dryline were westerly at 15 – 20 kts,

leading to relatively large convergence along the dryline. The National Weather Service in Norman, Oklahoma released a special weather balloon at 1700 UTC (Figure 4.1), revealing a "loaded gun" sounding with greater than 3000 J kg^{-1} MLCAPE and a capping inversion from 825 – 775 hPa. An elevated mixed layer from 750 – 600 hPa contributed to steep mid-level lapse rates around 9°C km^{-1}. Dewpoint depression at the surface of 5°C resulted in a relatively low mixed-layer LCL of 890 m. Vertical wind profiles exhibited a veering of wind with height along with 0-6 km wind shear of 52 kts and 0-1 km shear of 20 kts. This corresponded to SRH values of 131 m^2 s^{-2} and 156 m^2 s^{-2} from 0-1 km and 0-3 km, respectively.

The existing environment and potential for convective initiation along the sharp dryline led the Storm Prediction Center (SPC) to issue a moderate risk extending from north-central Texas to south-central Missouri including a 10% hatched tornado risk that encompassed the Oklahoma City metropolitan area. Though the SPC recognized risk for tornadoes especially from south-central to central Oklahoma, their overall confidence in a more substantial tornado threat was diminished due to 1) lack of low-level directional shear due to southerly, rather than southeasterly, surface winds and 2) the possibility of rapid upscale growth inhibiting time for isolated supercells.

At 1830 UTC, new convection initiated along the dryline bulge just south of the Chickasha, OK area. The initiation along the dryline bulge and the intersection between the dryline and the cold front would be essential in providing favorable environmental conditions necessary for tornadogenesis. Though convection that initiated earlier further to the south would attain supercellular characteristics, these supercells would remain non-tornadic. About 17 min later at 1847 UTC, additional convection

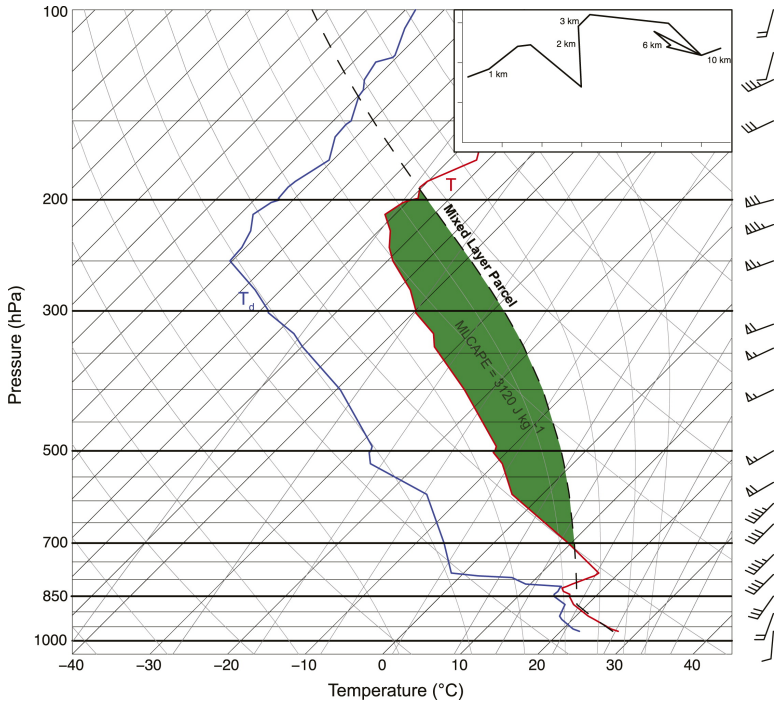

Figure 4.1: 1700 UTC OUN sounding on 20 May 2013. Graphic courtesy of Kurdzo et al. (2015).

initiated north of Chickasha, OK area and both newly developed cells track to the northeast towards the Oklahoma City Metro area. However, neither cell was able to mature and organize, leading to a broad area of relative weak Z_H. This diffuse precipitation continued until rapid growth occurred from 1908 to 1912 UTC, at which point the cells lift northward enough to interact with the SW – NE oriented boundary as evident on radar.

By 1921 UTC, explosive convection led to two mature cells, one to the north (storm A, Figure 4.2) and one to the south (storm B), each containing a large area of Z_H greater than 50 dBZ. Both cells were elongated in the E – W direction, illustrating strong wind shear contributing to rapid maturation. By 1934 UTC, both cells attain supercellular characteristics with a clear rotating mid-level updraft and associated

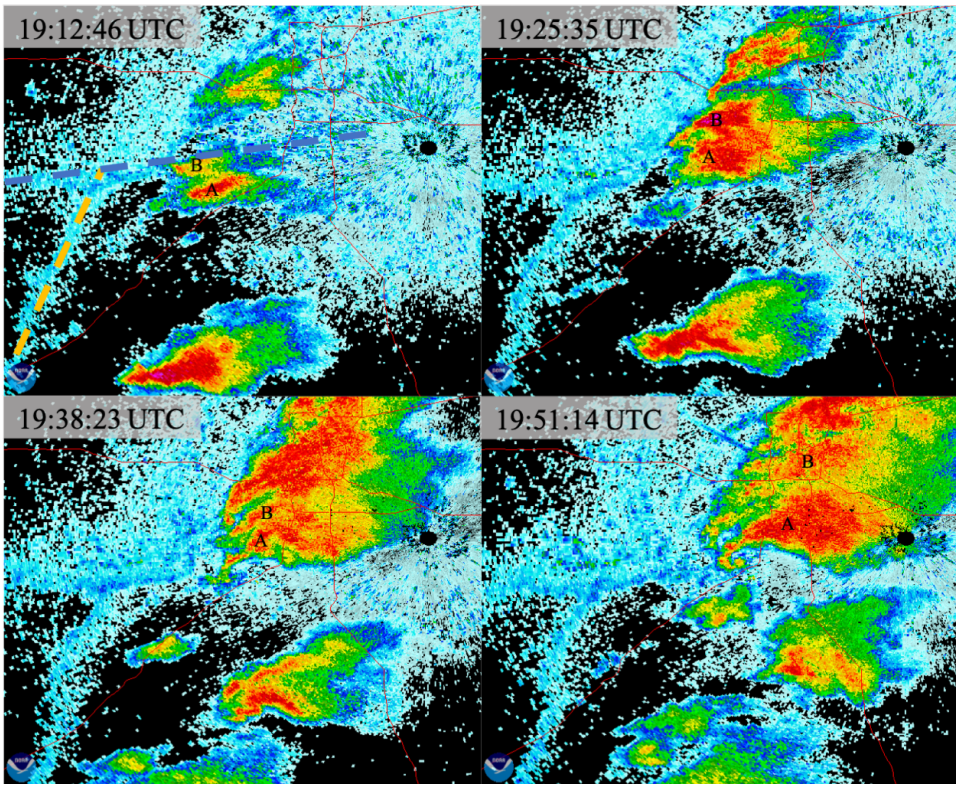

Figure 4.2: Sequential evolution of Z_H as observed by KTLX at 0.5° that shows the progression of the cells interactions with the dryline (dashed orange) and cold front (dashed blue). The supercell to be associated with the EF-5 tornado is labeled as storm A and the cell to the north is storm B.

hook echo appendage. However, storm B tracks north of the boundary prior to its storm motion deviating to the right, and thus enters an environment with conditions unfavorable to maintenance for supercells; thus, storm B weakens and loses its supercellular characteristics after 1938 UTC. On the other hand, storm A is able to make its right turn as the updraft intersects the boundary. Once the updraft becomes rooted on the boundary, boundaries are able to provide an additional source of low-level streamwise vorticity that storm A is able to ingest, combating the lack of low-level directional shear mentioned earlier (Markowski et al. 1998). Subsequent radar scans show a rapid strengthening of the supercell with a well-defined hook echo and clear

Z_H gradient along the leading edge of the FFD. As storm A strengthens and parallels the boundary, weak convection to the south tracks northeast with upper-level flow, resulting in a storm merger (not shown). The initial interaction of the supercell and the storm merger precedes tornadogenesis at 1956 UTC by a few minutes, possibly implying an influence from the storm merger on tornadogenesis mechanisms. Between 1956 and 2008 UTC, the supercell undergoes a rapid intensification of the low-level mesocyclone and tornado.

4.2 Polarimetric Supercell Evolution

The high spatiotemporal resolution of the PX-1000 allows for a thorough analysis of the evolution of polarimetric data as compared to the WSR-88Ds. The following section will highlight key times in which the supercell undergoes a period of important evolution, namely:

1. first storm merger which leads to the formation of the hook echo,
2. maturation of the supercell and hook echo inferred through processes such as increased drop size sorting and strengthening of the inflow region,
3. prevalence of numerous RFD surges with transient intensifications in ΔV_{max} and a detection of a pTDS,
4. dual-storm merger leading to heavy precipitation entrainment and subsequent tornadogenesis, and
5. rapid intensification of the tornado with a significant increase of lofted debris.

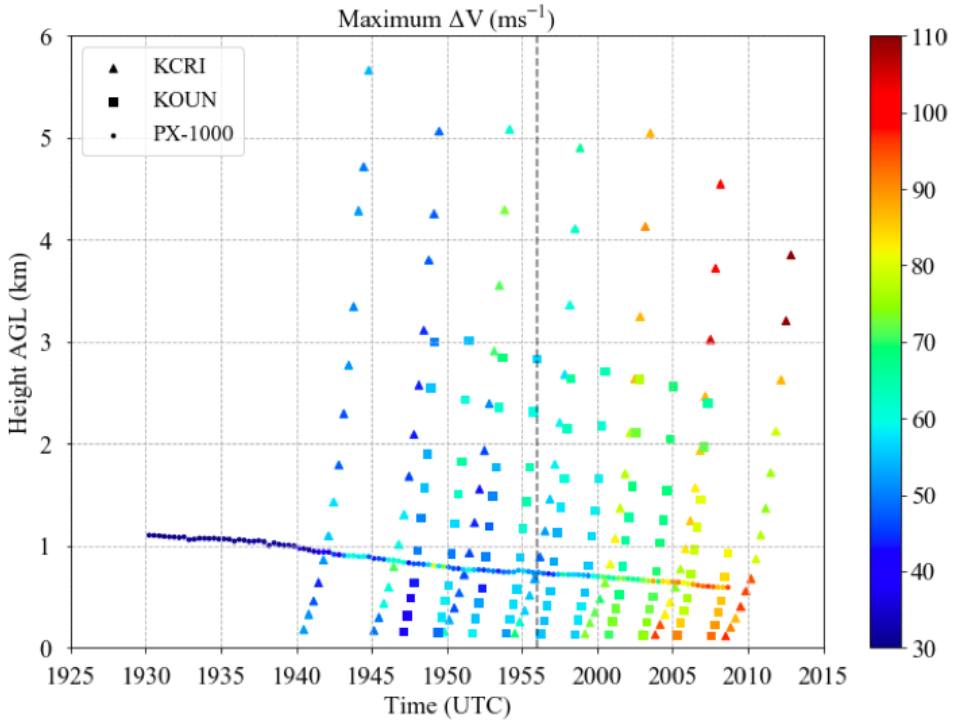

Figure 4.3: Time series of ΔV_{max} plotted above ground level (AGL) for PX-1000 (circles), KCRI (triangles), and KOUN (squares).

The first period between 1930:14 and 1934:12 UTC is defined by the rapid development of the hook echo appendage following a storm merger from the south (Figure 4.4). At the beginning of this period, the hook echo appendage of the supercell is marked by a wide appearance, with Z_H exceeding 30 dBZ stretching approximately 5 km in the east-west direction. As the secondary cell merges with the supercell, the hook echo rapidly narrows and strengthens, with Z_H exceeding 50 dBZ in some areas. Additionally, while the northern half of the appendage follows storm motion to the east-northeast, the southern periphery remains nearly stationary resulting in a north-south elongation. Note that at 1934:12 UTC, there is convection ongoing to the west of the center of the hook echo that is quite persistent through the next two analysis periods. This elongation in the E-W direction is likely a result of the

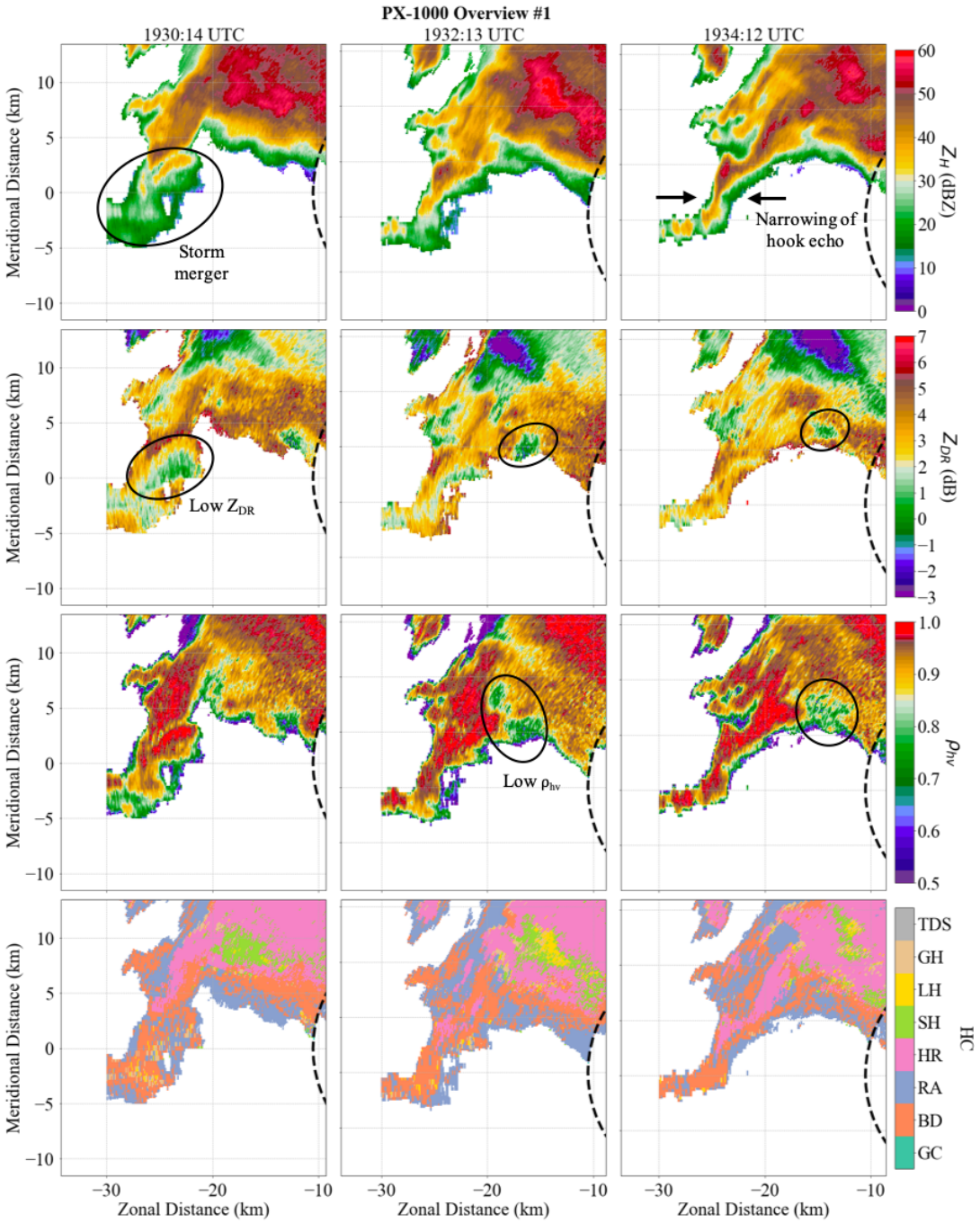

Figure 4.4: Three radar scans from PX-1000 of Z_H (first row), Z_{DR} (second row), ρ_{hv} (third row), and HCA (fourth row) documenting the evolution of the supercell during the first analysis period at 1930:14 (left column), 1932:13 (middle column), and 1934:12 UTC (right column). The dashed black line represents the extent of the blind range.

hook echo becoming rooted right on the boundary (as seen in Figure 4.2), allowing for additional convective development.

Analysis of Z_{DR} show that the secondary cell contains relatively low values of Z_{DR}, with some areas of negative Z_{DR}. Once the merger is complete, the hook echo is defined by both high Z_{DR} and ρ_{hv} values, suggesting a transition to larger drop sizes and the Z_{DR} arc wrapping into the hook echo (e.g., Palmer et al. 2011). Aside from the hook echo, the forward flank precipitation core also experiences a narrowing of the heaviest precipitation region, and the leading edge of the FFD becomes more well-defined. There is also a 90° notch at 1930:14 UTC located at the connection of the hook echo appendage to the main supercell, which translates within the supercell as an area of relatively low Z_H within the leading edge of the FFD. This remnant notch is also characterized by very low Z_{DR} and ρ_{hv} values, as low as -1 dB and 0.7, respectively.

During the subsequent analysis period from 1942:30 to 1946:29 UTC (Figure 4.5), the hook echo appendage takes on a more curved appearance with a consolidation of higher Z_H in addition to a well-defined inflow notch. Analysis of ΔV_{max} shows a transient increase to 60 $\mathrm{m\,s^{-1}}$ from approximately 1943 – 1945 UTC, which is also captured at lower-levels from KCRI (Figure 4.3). Z_{DR} shows an increase in organization of the Z_{DR} arc along the leading edge of the FFD with a well-defined Z_{DR} gradient oriented towards the leading edge. Moreover, high Z_{DR} values are advected into the appendage, evidence of strengthening inflow, consistent with the ΔV_{max} increase and detection of a few pTDS points through HCA analysis. Thus, Z_{DR} evolution indicates an increase in drop size sorting taking place through this

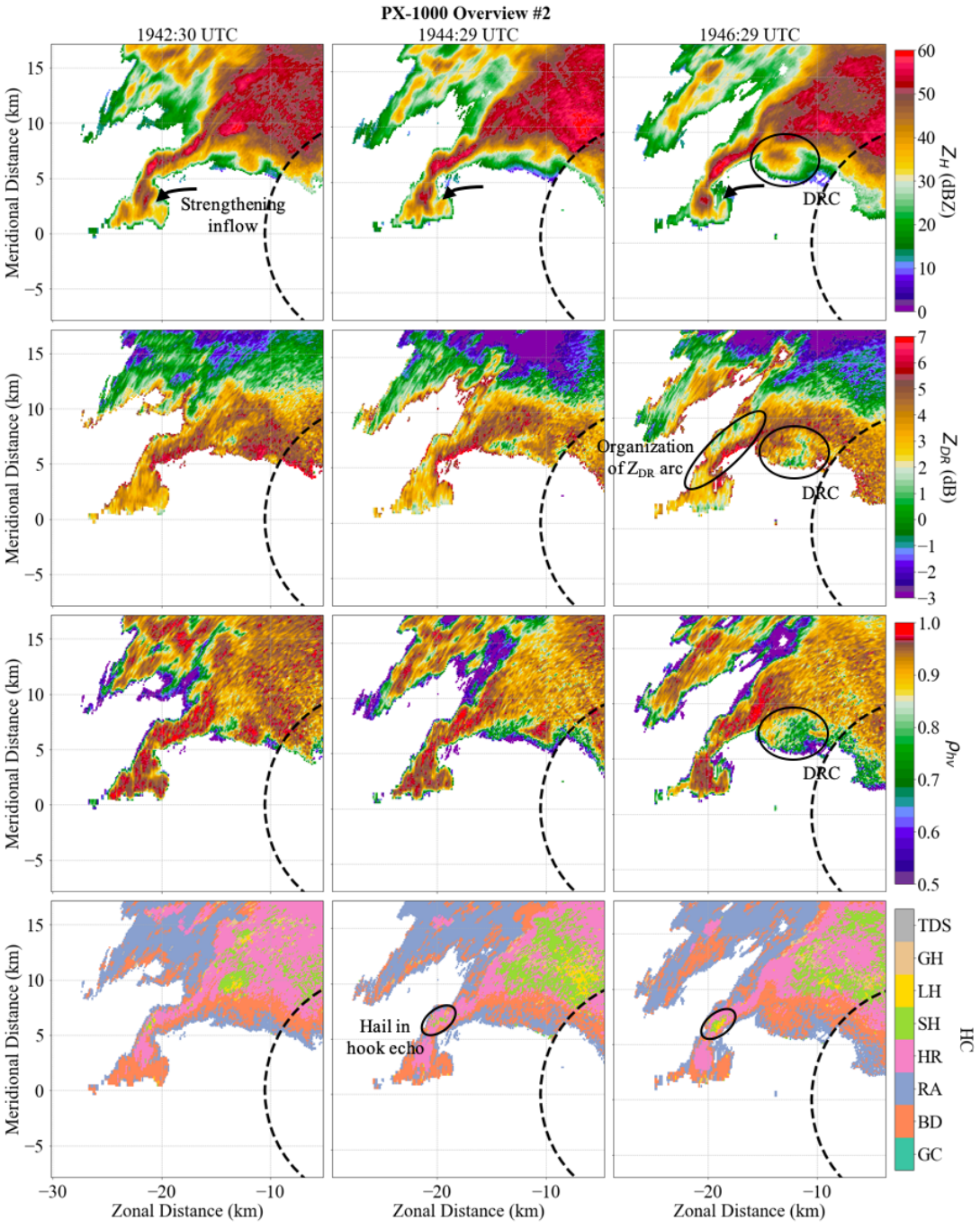

Figure 4.5: As in Figure 4.4, except for the second analysis period at 1942:30, 1944:29, and 1946:29 UTC.

analysis period. While ρ_{hv} within the hook echo appendage remains relatively high, indicative of rain-only processes, there is a small minimum located just in the middle of the appendage. This suggests a possible mixed-phase region, which is confirmed through HCA analysis with a small section of SH and LH collocated with the ρ_{hv} minimum and high Z_H, with a definite increase in spatial area of SH and LH points by the end of the analysis period.

Within the forward flank precipitation region, areas of heaviest precipitation are collocated with areas of ρ_{hv} that are slightly lower than surrounding areas, with values less than 0.9. This is further suggestive of possible melting hail mixed in with liquid precipitation, and seems to be confirmed through the HCA with mostly SH points trickled into the forward flank region. Additionally, at the end of the analysis period, there is a clear descending reflectivity core (DRC) that is distinguishable through a region of Z_H maximum located ahead of the leading edge of the FFD. The DRC is also marked by lower Z_{DR} and ρ_{hv} values compared to the adjacent Z_{DR} arc.

The third analysis period from 1949:08 to 1953:09 UTC is marked by multiple RFD surges coincident with transient intensifications in ΔV_{max} (Figure 4.3 and 4.6). PX-1000 ΔV_{max} analysis shows two clear maxima, one which occurs at 1949 UTC and another at 1952 UTC, embedded within a background steady increase as the broad mesocyclone contracts into a much tighter circulation especially towards the end of this analysis period just before tornadogenesis. The RFD surges may play a role in these transient intensifications, and inbound velocities traversing across the hook echo. These RFD surges will be the focus of the next section and will be analyzed in higher temporal detail. Z_{DR} and ρ_{hv} within the hook echo ball begin to decrease,

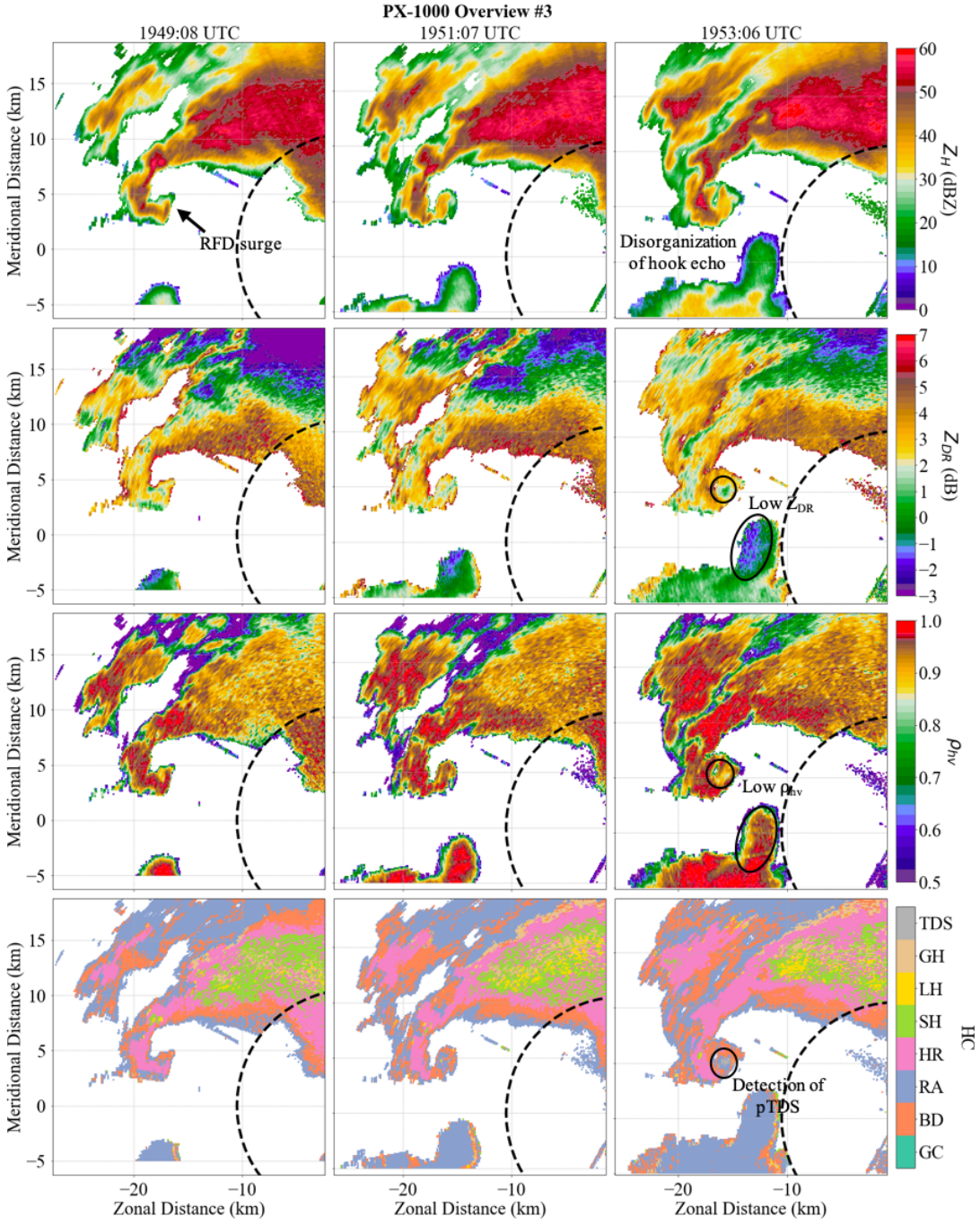

Figure 4.6: As in Figure 4.4, except for the third analysis period at 1949:08, 1951:07, and 1953:06 UTC.

resulting in the detection of additional pTDS points using the HCA. However, Z_H values are lower than typical TDS thresholds and are more consistent with storm-scale debris signatures observed in inflow. In a damage survey conducted by the National Weather Service, 70 damage indicators to vegetation and residential property were noted prior to tornadogenesis (Atkins et al. 2014; Burgess et al. 2014). Thus, the pTDS is likely to be a result of 1) strong vertical motions and concentrated inflow associated with strengthening low-level rotation acting to enhance lofting of light debris such as leaves and 2) hydrometeor size mixing from RFD surges, the process of which is detailed and explained further in section 4.3.

During this analysis period, the supercell remains quasi-steady with consistent heavy precipitation (Z_H greater than 50 dBZ) marked by an area of SH points in the HCA located in the middle of the forward flank precipitation region. Additionally, the Z_{DR} arc remains well-defined alluding to drop size sorting playing a significant role. While they have not yet occurred, two storm mergers, one from the south and one impinging from the northwest side, are the beginning to interact with the supercell.

This analysis period from 1954:46 to 1958:44 UTC is marked by a storm merger with a secondary cell to its northwest, associated with fairly robust convection and Z_H exceeding 50 dBZ. There is a simultaneous storm merger that initially merges with the eastern periphery of the hook echo, and is defined by stratiform-like precipitation with lower Z_H mainly less than 30 dBZ. While the convective storm merger is associated with high values of Z_{DR} and ρ_{hv} including its own Z_{DR} arc, a weaker storm to the south merges and is characterized by lower values of Z_{DR} (possible non-meteorological scatterers). During the storm merger, the hook echo attains a more

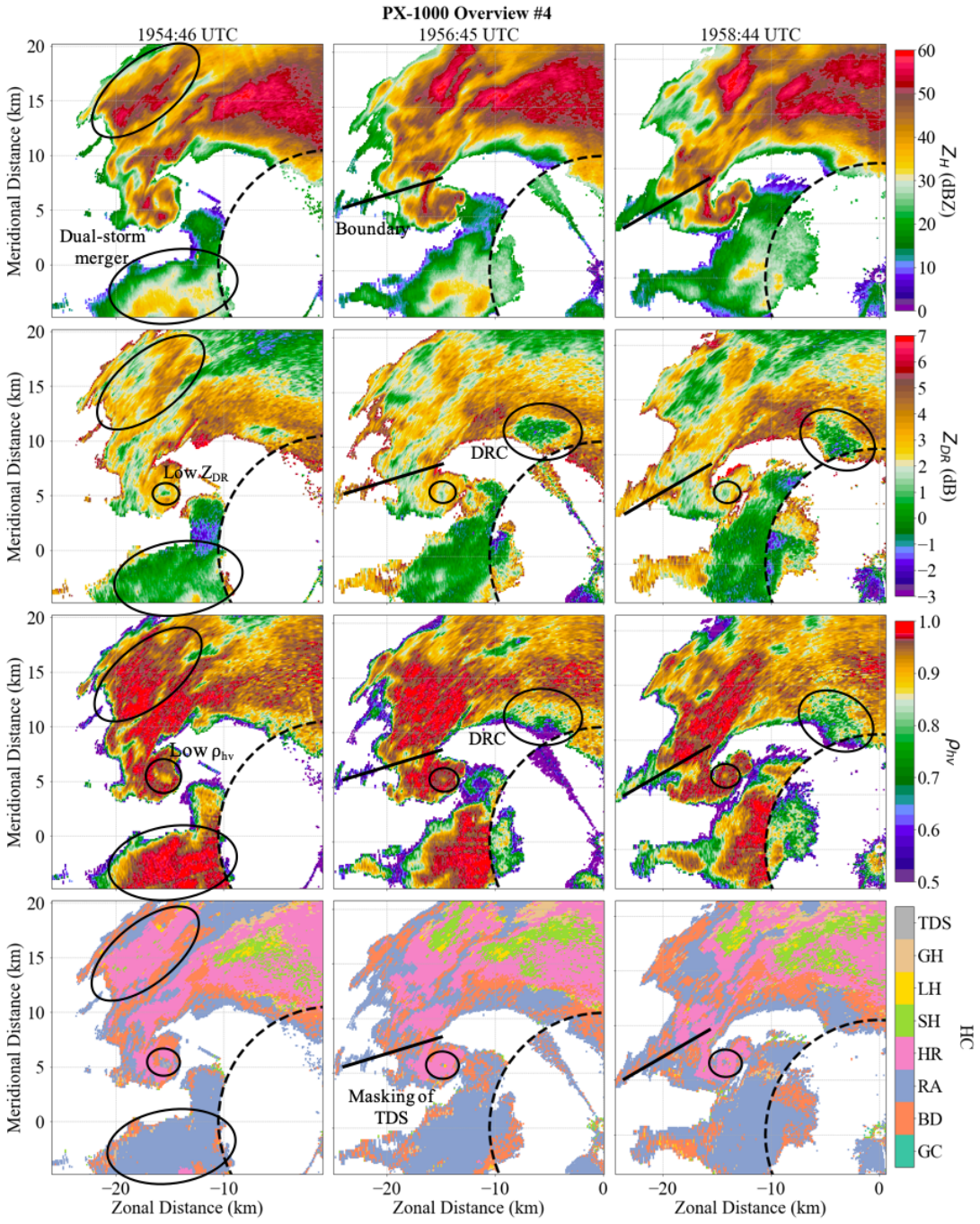

Figure 4.7: As in Figure 4.4, except for the fourth analysis period at 1954:46, 1956:45, and 1958:44 UTC.

disorganized overall structure. However, a band of heavy precipitation (Z_H greater than 50 dBZ) and large drops encircles the developing tornado fully enclosing it by 1958 UTC. ΔV_{max} shows a transient intensification to $\sim$70 m s^{-1} just after tornadogenesis (1956 UTC) and another intensification at the end of this analysis period, captured both by PX-1000, and KCRI and KOUN through the entire column. Ironically, the pTDS points captured by HCA becomes masked by excessive precipitation entrainment as tornadogenesis occurs. HCA for WSR-88Ds show a similar masking from precipitation (not shown), with a slight decrease in the number of TDS points for KTLX and KOUN just at the time of tornadogenesis; while KCRI does not show a decrease, this is likely due to insufficient temporal resolution, as tornadogenesis occurs in between scans with the closest being 2 min prior to tornadogenesis.

Elsewhere in the supercell, HCA indicates a possible decrease in hail productivity within the FFD around the time of tornadogenesis when compared to the previous analysis period, consistent with results from Broeke (2017). Additionally, there is another notable DRC that starts at the beginning of the analysis period about 15 km to the east-northeast of the hook echo region, with the spatial extent growing through the duration of the analysis period. Similar to the first noted DRC, the Z_{DR} and ρ_{hv} values are low, down to -1 dB and 0.7, respectively.

The last analysis period, from 2000:04 to 2004:23 UTC, is defined by rapid intensification of the tornado. Analysis of ΔV_{max} clearly shows a consistent (rather than transient) strengthening of the velocity couplet, including a detection of ΔV_{max} exceeding 90 m s^{-1} just above the surface from KCRI and KOUN. While the southern, stratiform storm merger is still occurring during this period, the hook echo appendage

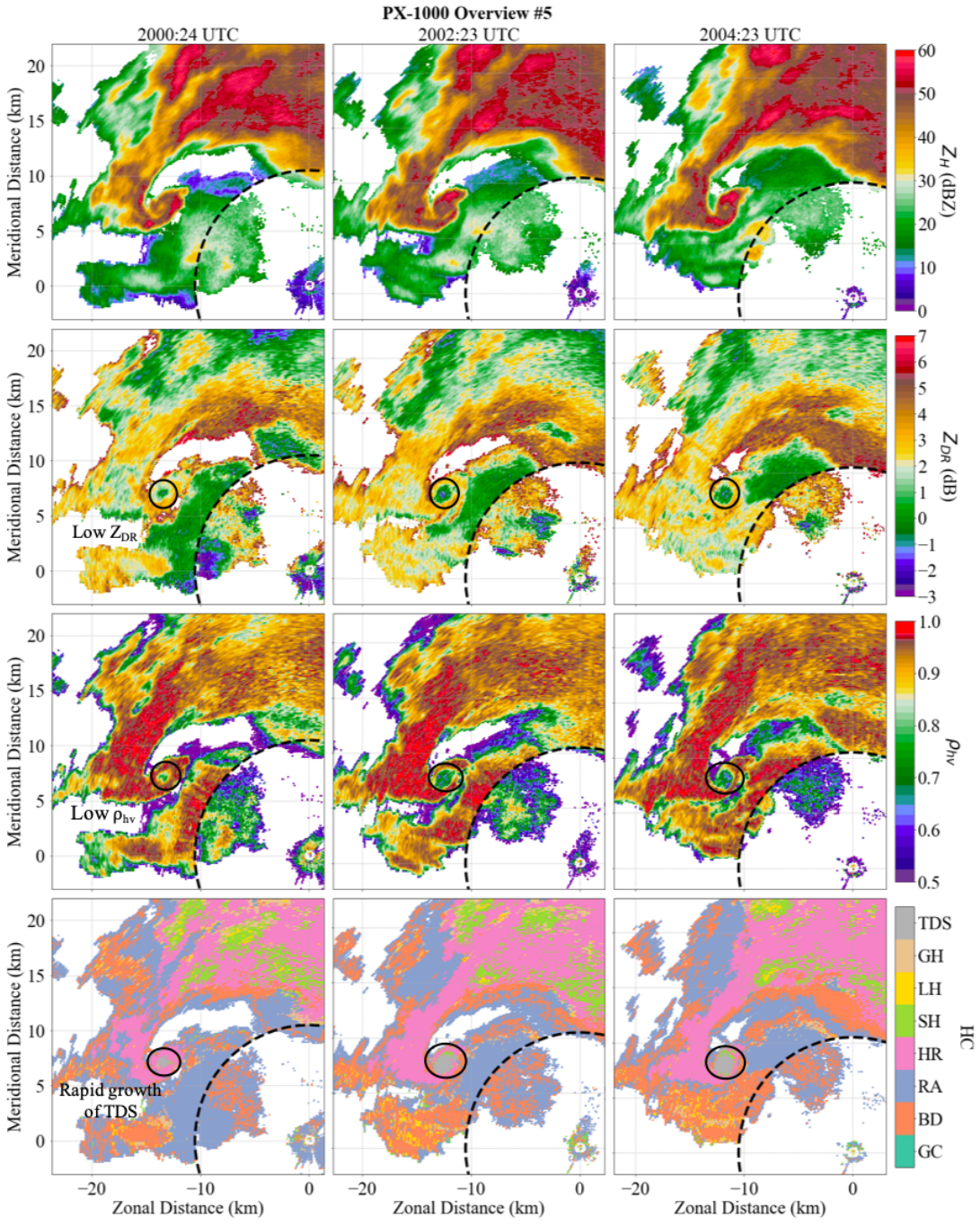

Figure 4.8: As in Figure 4.4, except for the fifth analysis period at 2000:04, 2002:23, and 2004:23 UTC.

no longer has a disorganized appearance, and the hook echo "ball" continues to take on a more circular and symmetrical appearance. As the amount of lofted debris begins to overcome precipitation entrainment effects, both lower values of Z_{DR} and ρ_{hv} within the center of the tornado begins to drop and increase in spatial extent radially outward. This leads to a drastic increase in the detection of TDS points using HCA.

4.3 Rear-Flank Downdraft Surges

Previous studies have suggested that polarimetric characteristics of the hook echo are associated with storm-scale processes. The formation of the hook echo is a product of a strengthening mesocyclone that results in precipitation being wrapped cyclonically around the periphery of the updraft and descending towards the surface. Thus, hook echo characteristics are inherently related to storm-scale processes, including mesocyclone intensity, updraft strength, and low-level precipitation attributes. Picca et al. (2010) found that low-level precipitation intensifies prior to updraft strengthening as inferred from the Z_{DR} column. Ambient wind shear (SRH) contributes to drop size sorting of precipitation within the supercell, resulting in varying spatial distributions and gradients in Z_{DR}, i.e., the Z_{DR} arc (Kumjian 2013). Similarly, air that is forced to descend due to impedance of flow by the updraft can manifest as RFD surges which are detectable through rapid changes in precipitation within the hook echo (Kumjian 2011). However, because RFD surges can occur on short timescales, sufficient spatial and temporal resolution radars are necessary to resolve such a finescale process. On 20 May 2013, the PX-1000 was able to capture three distinct RFD surges

that occurred during the analysis period at 1946:09, 1952:27, and 1957:05 UTC, the evolution of which is shown in Figures 4.9, 4.10, and 4.11, respectively. These times correspond to the time at which the RFD surges outwards the furthest, eventually catching up to and overtaking the rear-flank gust front (RFGF), hereafter referred to as the times of the RFD maximum.

Since the RFD surges are a product of descending air resulting in enhanced outflow, these features are most apparent using V_R and are characterized by inbound radial velocities traversing the hook echo, surging east of the velocity couplet (second row, Figures 4.9 – 4.11). The RFD surge is typically associated with an eastward acceleration of the eastern periphery of the hook echo precipitation region. Within the hook echo, there are two distinct processes which are leading to a unique drop size distribution (DSD; Figure 4.12). Namely, drop size sorting within the leading edge of the hook echo (closest to the inflow region) results in large drops and high values of Z_{DR} – an extension of the Z_{DR} arc into the hook echo (Kumjian 2011; French et al. 2015). The second process is a warm rain / dynamic forcing mechanism which results in smaller droplets and relatively low values of Z_{DR} to descend to the surface via the RFD and concentrate along the western and southern peripheries of hook echo (third row, Figures 4.9 – 4.11). This leads to a gradient of Z_{DR} which is oriented towards the leading edge of the hook echo.

During RFD surges, the Z_{DR} gradient also surges and wraps cyclonically around the low-level mesocyclone. Additionally, strong near-surface winds associated with the RFD surge may loft dust and loft small debris such as grasses and leaves, resulting in decrease in ρ_{hv} around the time of the RFD maximum (fourth row, Figures 4.9 and

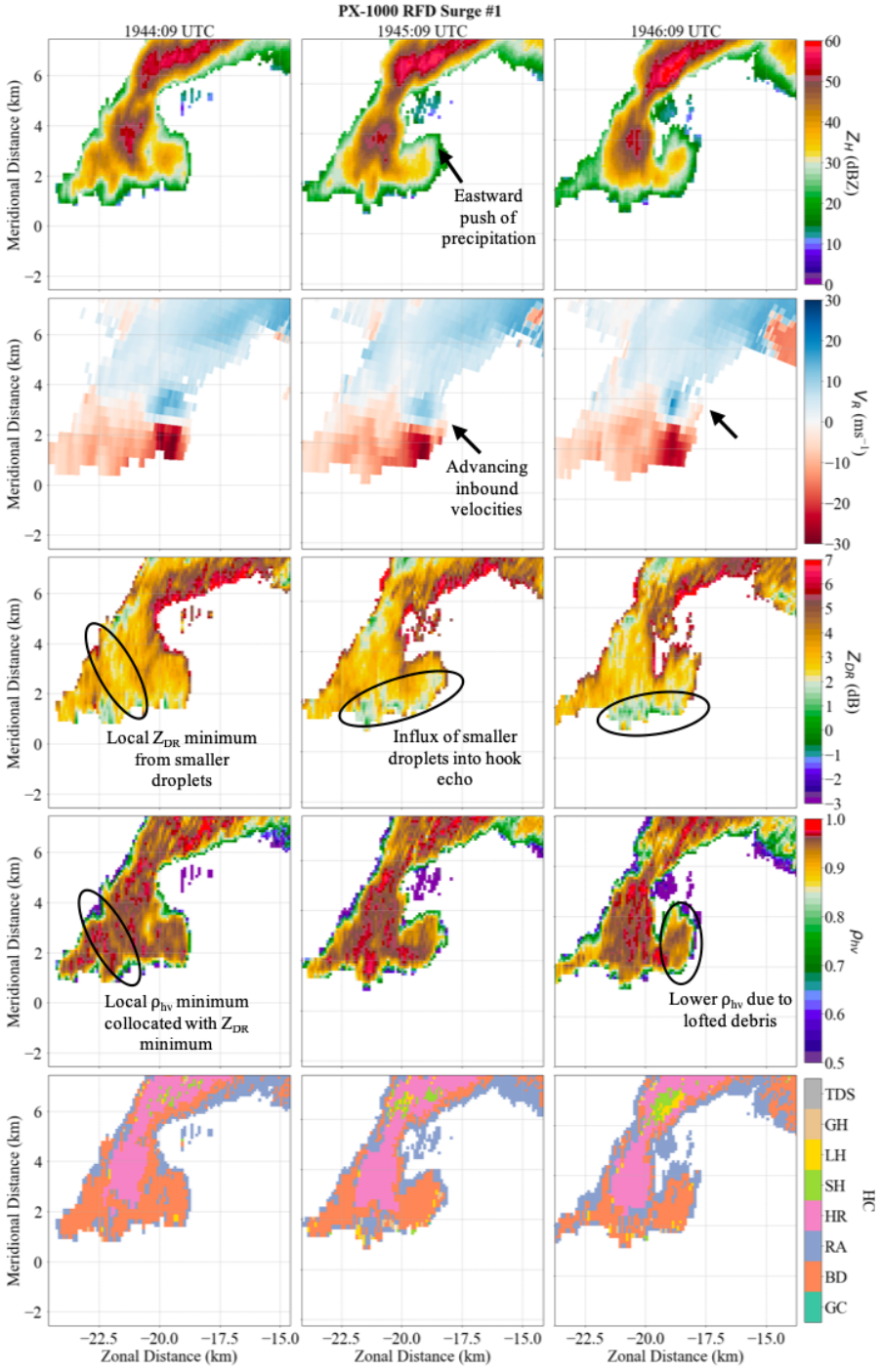

Figure 4.9: From top to bottom row: Z_H, V_R, Z_{DR}, ρ_{hv}, and HCA from PX-1000 for three subsequent times — from left to right column, 1944:09, 1945:09, and 1946:09 UTC — highlighting the first occurrence of an RFD surge. Annotations detail polarimetric characteristics associated with the evolution of the RFD surge.

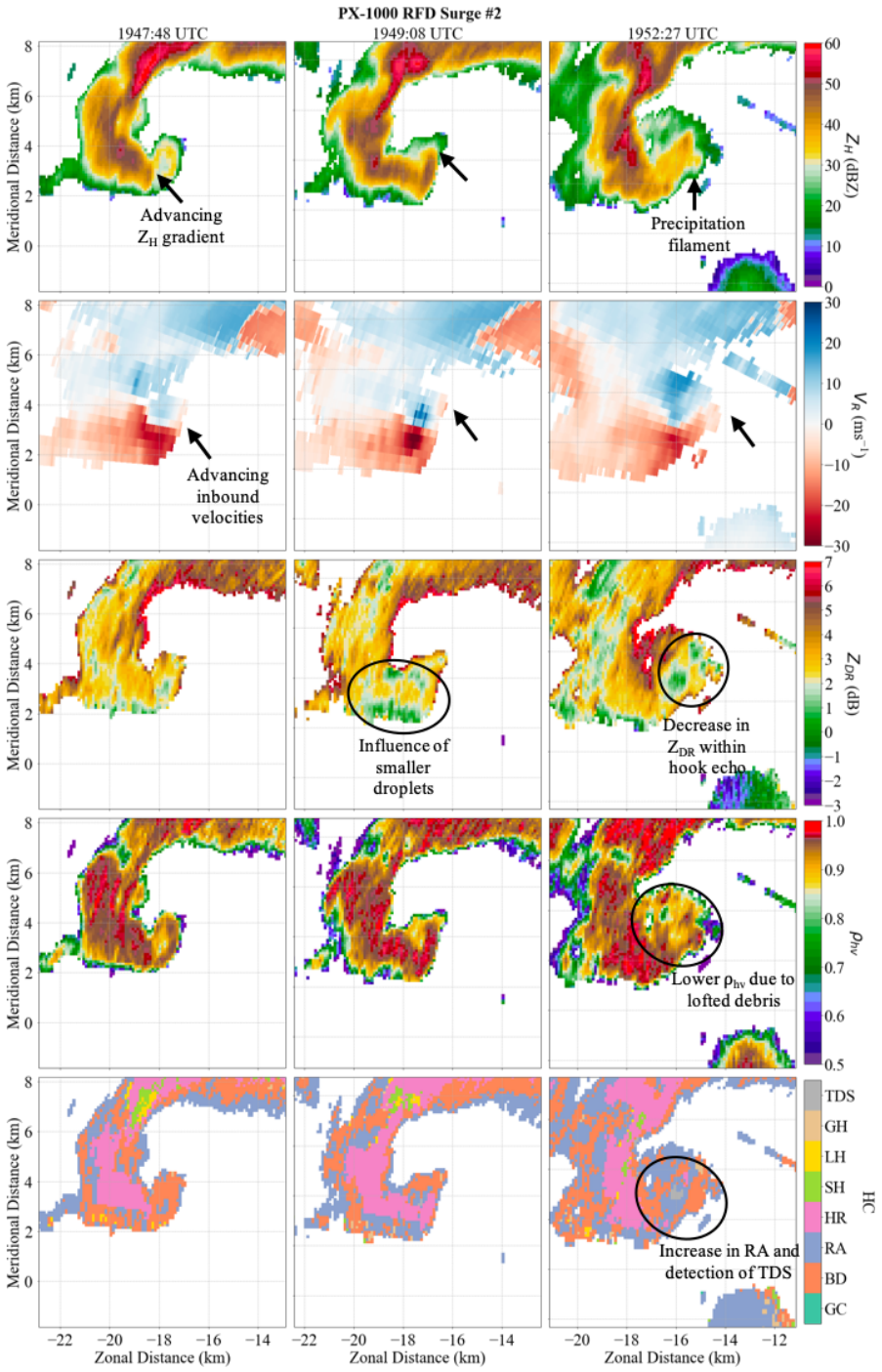

Figure 4.10: As in Figure 4.9, except for the second RFD surge at 1947:48, 1949:08, and 1952:27 UTC.

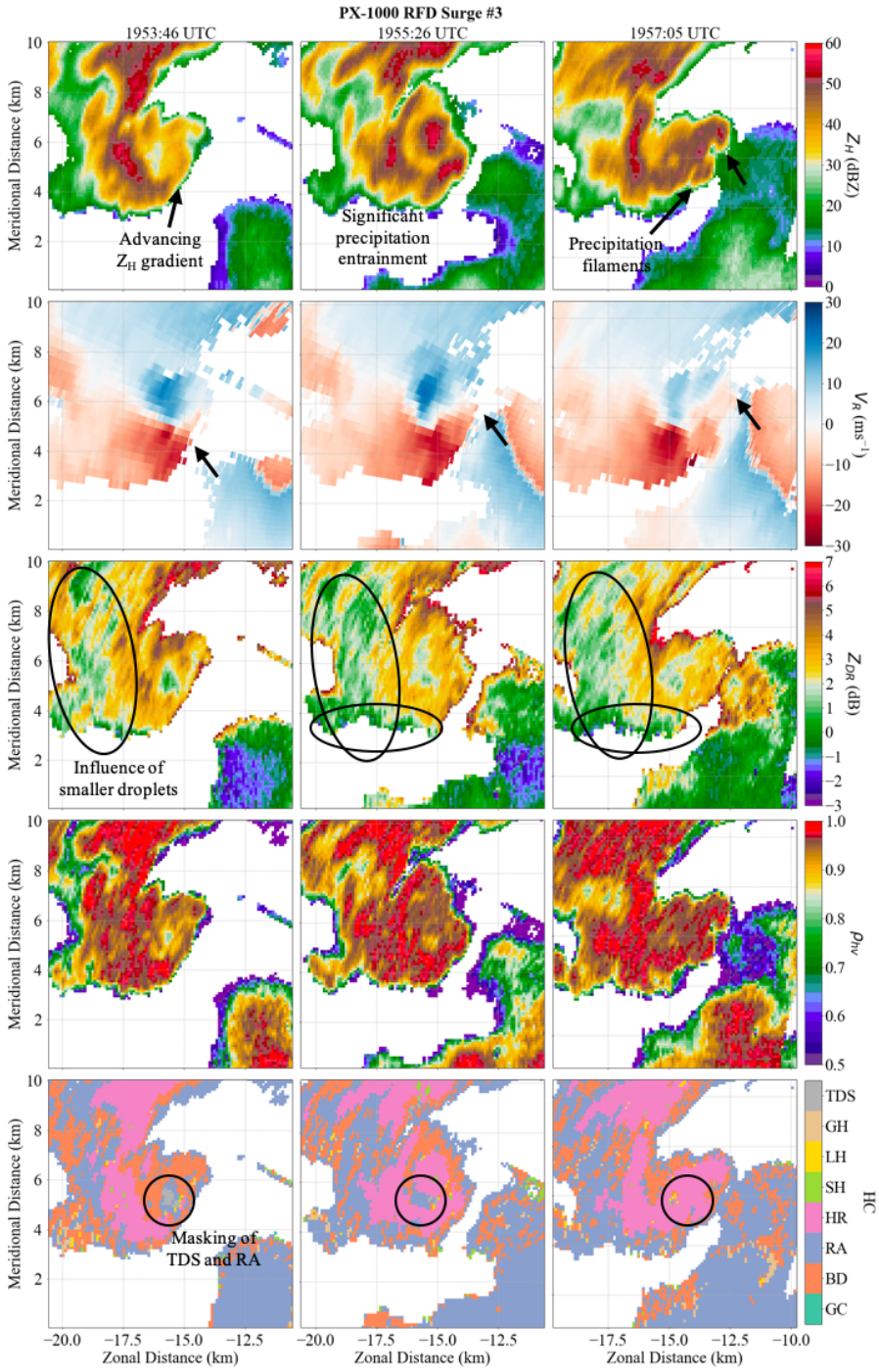

Figure 4.11: As in Figure 4.9, except for the third RFD surge at 1953:46, 1955:26, and 1957:05 UTC.

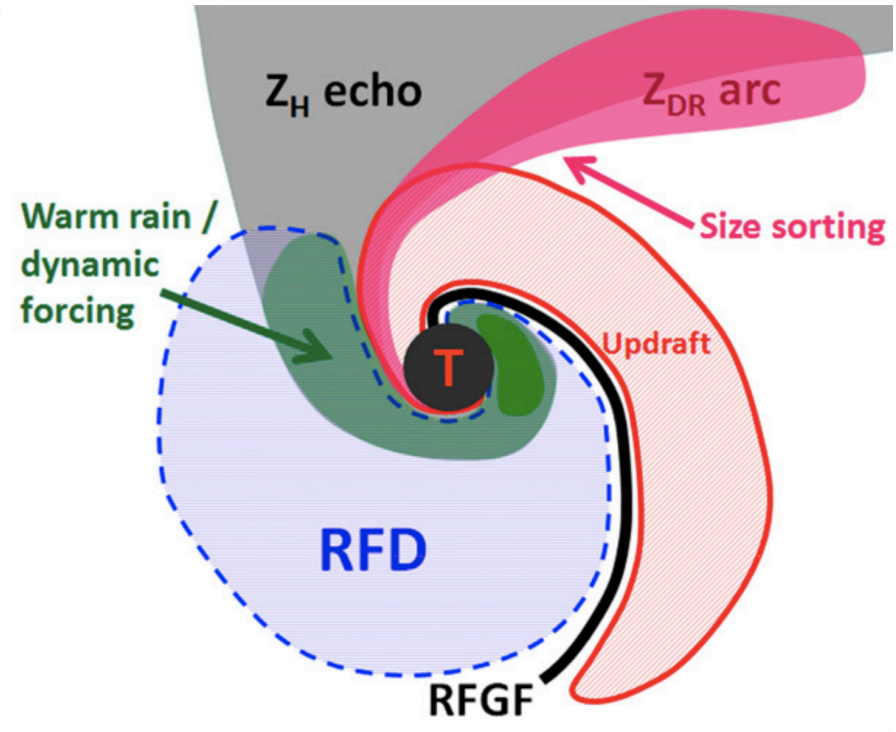

Figure 4.12: Schematic of the supercell hook echo showing the location of the RFD (hatched blue), updraft (hatched red), large drops associated with the Z_{DR} arc (solid red), and small drops associated with warm rain and dynamic forcing (solid green). Figure is adapted from Kumjian (2011).

4.10). Lofting of debris may also manifest as a drop in Z_{DR} (third row, Figure 4.10)—however, because preferred orientation of debris particles more obscure, patterns in ρ_{hv} are preferable in assessing the times of the RFD maximum. In the second and third RFD surges, the surge is strong enough such that high values of Z_H that exist within the hook echo appendage are noted to advance cyclonically around the hook echo (first row, Figure 4.10 and 4.11), noted as an advancing Z_H gradient. Hydrometeors which are advected a significant distance away from the velocity couplet can manifest as precipitation filaments which extend off the periphery of the hook echo (first row, Figures 4.10 and 4.11).

The 20-s temporal resolution of the PX-1000 allows for the tracking of the Z_H gradient in the second RFD surge, which takes about a minute and a half to completely enclose the hook echo leaving a WEH at the center (Figure 4.13). The advanced Z_H gradient is collocated with a Z_{DR} gradient that also advances during the RFD surge and becomes more well-defined, with lower values to the north and south of the Z_H maximum, which contains higher values of Z_{DR}. As the rain curtain wraps around the hook echo, there is a brief increase in ΔV_{max} at $\sim$1949 UTC which exceeds tornado intensity but is not sustained (Figure 4.3), consistent with Davies-Jones (2008) who found rain curtains can increase convergence and instigate tornadogenesis. Additionally, HCA detects an increase in pTDS points as the Z_H gradient begins to advance, with a local maximum coincident with ΔV_{max} (Figure 4.14b). Since the transient intensification of ΔV_{max} is relatively large (over 80 $\mathrm{m\,s^{-1}}$), one could argue with the presence of pTDS points and a relatively dense area of damage indicators associated

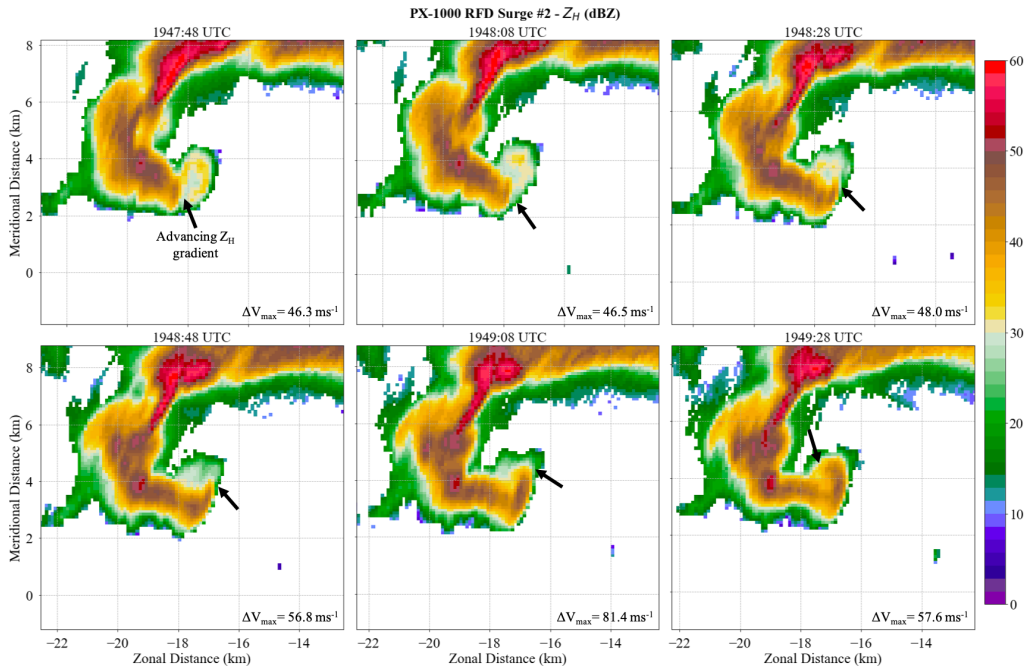

Figure 4.13: Six subsequent radar scans from PX-1000 of Z_H every 20 seconds from 1947:48 to 1949:28 UTC highlighting the advancing Z_H gradient during the second RFD surge.

with this RFD surge, that a brief tornado may have occurred, but ultimately resulted in the failure of the tornado to sustain itself.

To quantify these changes, the median of Z_{DR} and ρ_{hv} within 2 km of the hook echo center point is shown in Figure 4.14a, using data points with Z_H greater than 20 dBZ and ρ_{hv} above 0.7. These thresholds, as well as the use of a median, were chosen to eliminate possible biases from noisy data. Figure 4.14a shows two clear local minima in the median of ρ_{hv} dropping down to values of 0.92 and 0.90 at approximately 1946 and 1952 UTC, respectively, which corresponds to the first two RFD maxima. Because Z_{DR} shows an overall decreasing trend from 1940 to about 1950 UTC, likely due to supercell maturation and increased drop size sorting advecting larger drops further downshear of the updraft, it is quite difficult to discern areas in which the Z_{DR}

drastically differs from the background pattern. Temporal evolution of HCA (Figure 4.14b) shows a steeper drop in BD relative to the overall background decrease and a sharp increase in RA, representative of smaller drops, at around 1947 UTC, which corresponds to just after the first RFD maximum. This is consistent with Kumjian (2011) as small drops are advected into the hook echo coincident with the RFD surge maximum.

The combination of lower ρ_{hv} and Z_{DR} from light debris causes a detection of a non-zero number of pTDS points starting from 1946 UTC, with the initial increase at 1947 UTC and a much larger and more significant increase peaking around 1953 UTC (last row, Figure 4.10), both of which occur just after the RFD maximum. Both are also associated with transient increases in ΔV_{max}, the latter of which is also captured by KCRI just above the surface. Findings from Ortega et al. (2014) also note an increase in ΔV_{max} just prior to 1953 UTC that coincided with confluent damage / tree fall patterns analyzed using high-resolution satellite imagery, suggestive of a weak, short-lived vortex (Karstens et al. 2013). These findings were further supported by video evidence that captured a brief debris cloud near the ground. However, despite numerous transient increases in ΔV_{max} and detection of pTDS points by HCA, the official start time of the tornado was set to 1956 UTC as a result of inconclusive evidence of earlier formation.

The last RFD maximum occurs at approximately 1957:05 UTC and is also detectable using both V_R and an advancing Z_H gradient, with areas greater than 60 dBZ observed to wrap cyclonically around the couplet (first and second row, Figure 4.11). This RFD surge is arguably the longest in duration, with the Z_H gradient starting to

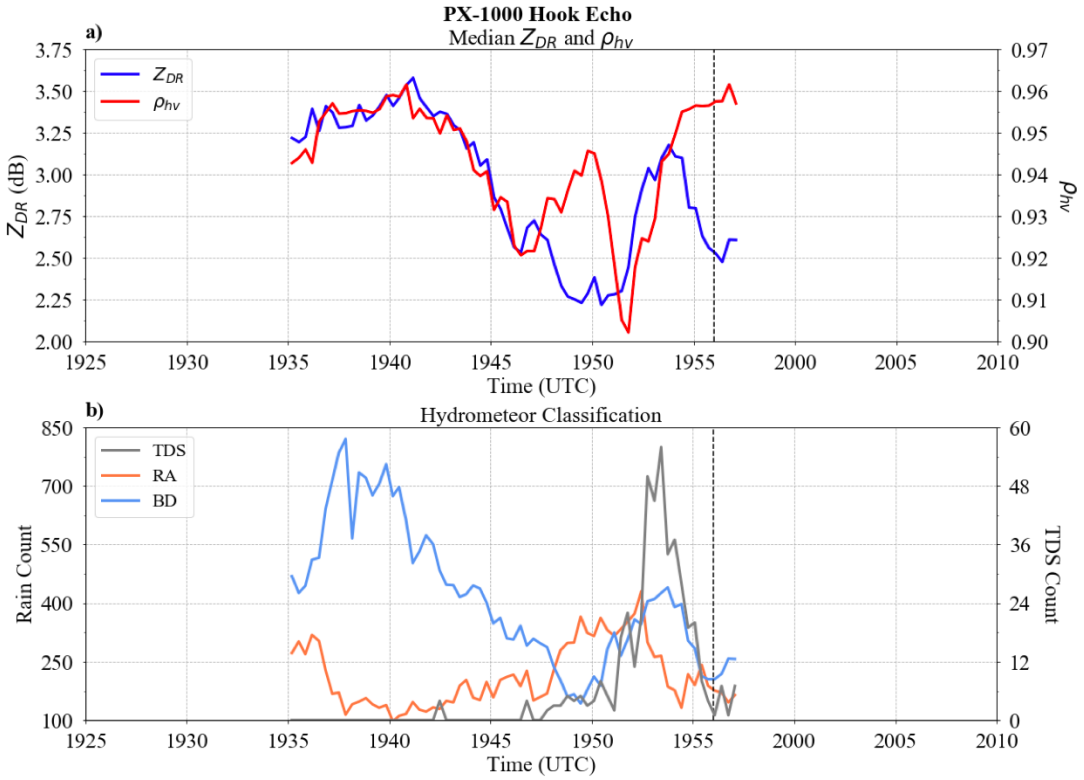

Figure 4.14: a) Time series of the median Z_{DR} (blue) and ρ_{hv} (red) within the hook echo from 1935 to 1957 UTC and b) count of interpolated grid points where the HCA detects TDS (gray), RA (orange), and BD (blue) from PX-1000.

advance at 1953 UTC and lasting through tornadogenesis. Unlike the first two surges in which Z_{DR} patterns were difficult to discern, the third RFD surge is associated with a clear drop in Z_{DR}, likely because more substantial debris from the tornado is beginning to be lofted. Interestingly, the median ρ_{hv} within the hook echo does not drop by any significant amount and remains near 0.96. This is likely the result of the hook echo becoming heavily entrained by precipitation during this time as a result of storm merger influences from the southwest (first row, Figure 4.11). As a result of such high ρ_{hv}, the HCA detects only a handful of TDS points during the first minutes after tornadogenesis (Figure 4.14b) and quickly becomes masked by HR in the HCA (last row, Figure 4.11).

Chapter 5

Volumetric Analysis of the Z_{DR} and K_{DP} Signatures

This chapter analyzes Z_{DR} and K_{DP} signatures to examine their relationship to dynamical processes occurring within the supercell. The analysis is segmented by processes existing in the horizontal and vertical, i.e., the Z_{DR} arc and K_{DP} foot, and Z_{DR} and K_{DP} columns, respectively. The first part of the analysis will be focused on the Z_{DR} arc and K_{DP} foot to analyze lower-level processes (Figure 5.1a). The second part will look at the vertical distribution of the Z_{DR} column and K_{DP} column to infer updraft characteristics (Figure 5.1b).

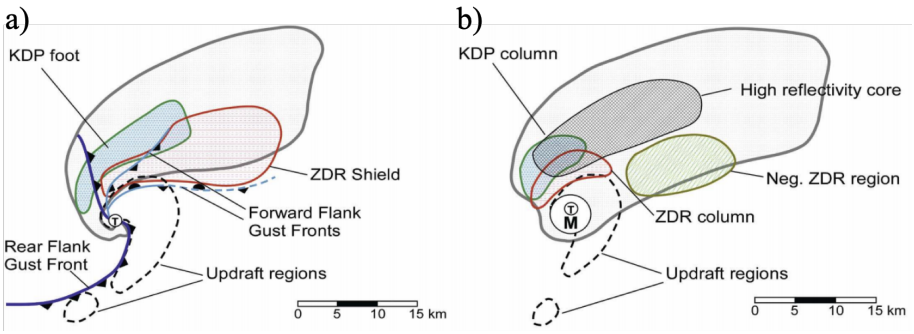

Figure 5.1: Schematic illustrating a) lower-level and b) upper-level polarimetric signatures in a supercell. Graphic courtesy of Romine et al. (2008).

5.1 Z_{DR} Arc and K_{DP} Foot

Because PX-1000 becomes heavily attenuated especially within the FFD precipitation core where both Z_{DR} arc and K_{DP} foot will be analyzed, the following analysis will rely on S-band radars: KTLX and KOUN. Although the temporal resolution of KTLX and KOUN is lower than PX-1000, they allow for analysis of volumetric characteristics of both enhancement regions and are less susceptible from attenuation. Characteristics of enhancement regions to be analyzed include the volumetric extent, depth, separation orientation and distance between the two centroid, and the centroid tracks. Recall that the method for detection of the enhancement region is one of a constant threshold, namely, Z_{DR} greater than 3.5 dB and K_{DP} exceeding 1.5 dB km^{-1}. Because data for KTLX is available from about 1930 – 2008 UTC and KOUN data is limited to 1947 – 2007 UTC, the latter is utilized to verify patterns found in the KTLX data with faster temporal sampling (2 – 3 min).

Because Z_{DR} arc and K_{DP} foot are generally observed in the lowest 2 km (e.g., Kumjian and Ryzhkov 2008, 2009), only data below 2 km are considered for this analysis. The time series of enhancement region characteristics are shown in Figure 5.2 while the plots of the enhancement region depth for each KTLX scan is shown in Figures 5.3 and 5.4. Using KTLX data, both the Z_{DR} arc and K_{DP} foot show an increase in volumetric extent from 1930 to 1946 UTC (Figure 5.2a) with the radar scans for this time period shown in Figure 5.3. While the depth of the K_{DP} foot also increases during this period, the depth of the Z_{DR} arc remains relatively steady or decreases slightly. Thus, while the both Z_{DR} arc and K_{DP} foot are increasing in

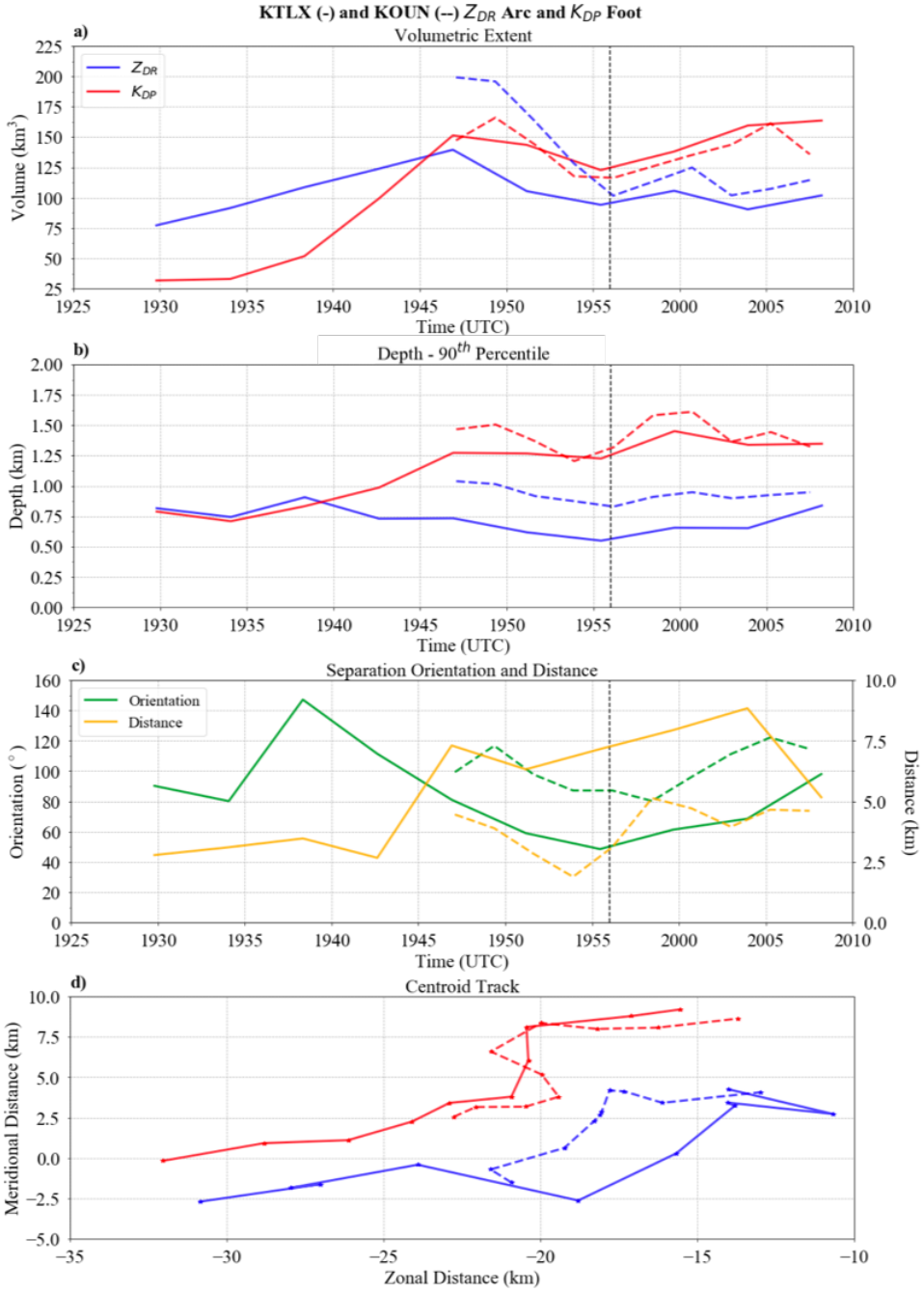

Figure 5.2: Using KTLX (solid lines) and KOUN (dashed lines): a) Volumetric extent of the enhancement regions, b) 90^{th} percentile of the depth of the enhancement region, c) separation orientation and distance using the centroids, and d) the track of the Z_{DR} arc and K_{DP} foot centroids using the depth field.

areal extent, only K_{DP} foot is becoming deeper with time, reaching about 1.3 km by 1946 UTC compared to about 0.75 km for the Z_{DR} arc. The relative shallowness of the Z_{DR} arc compared to the K_{DP} foot suggests that size sorting is occurring in a relatively shallow layer.

This pattern prior to 1946 UTC is confirmed through Figure 5.3; while both Z_{DR} arc and K_{DP} foot grow in size to encompass the majority of the FFD, only K_{DP} foot steadily deepens during the latter half of the this time period with a consolidation to the northeast (upshear) of the updraft while Z_{DR} arc arguably becomes more diffuse. Physically, it is likely that the larger drops (high Z_{DR}) are being dispersed farther from the updraft while the small and medium droplets are becoming concentrated downshear of the updraft, resulting in a high liquid water content and K_{DP} values. The track of the K_{DP} centroid from 1930 – 1946 UTC is relatively steady, moving to the east-northeast (similar to storm motion; Figure 5.2d). The Z_{DR} centroid is slightly more variable; while general movement is also to the east-northeast, the third scan shows a reversed movement to the southwest as a result of a region of high Z_{DR} near the hook echo appendage, which results in an increase of separation orientation (Figure 5.2c). The last scan at 1946 UTC shows a slight southward movement of the Z_{DR} centroid due to high Z_{DR} values that appear associated with a southward bulge in the leading edge of the FFD. Because of the faster forward motion of the Z_{DR} centroid relative to the K_{DP} centroid at the end of this period (Figure 5.2d), the separation orientation and distance show a decreasing and increasing pattern, respectively (Figure 5.2c). The maximum in separation orientation occurs at 1938:21 UTC ahead

of transient intensifications in ΔV_{max} which indicates that the low-level mesocyclone begins to intensify once separation orientation begins to steadily decrease.

The next five KTLX scans from 1951 to 2008 UTC are characterized by a relative steadiness in both the volumetric extent and depth of the Z_{DR} arc and K_{DP} foot (Figure 5.2a-b). Only the volumetric extent for Z_{DR} arc shows a decrease during the first half of this time period. Additionally, the K_{DP} foot remains deeper than the Z_{DR} arc for the entire period, which is likely a result of small and medium sized drops associated with the K_{DP} foot encompassing a larger depth than large drops associated with the Z_{DR} arc as speculated before. All of these patterns are confirmed performing the same analysis with KOUN data which is in agreement with patterns from KTLX. The first half of this period is also characterized by a leftward turn in both Z_{DR} arc and K_{DP} foot, the latter having a more significant turn with an almost due north track per KTLX analysis (Figure 5.2d). Investigating Figure 5.4 further, the northward turn of the K_{DP} foot is owing to an increased prevalence of drop size sorting, with further consolidation of large concentration of small to medium sized drops further northward resulting in increased liquid water content within the FFD. Additionally, the K_{DP} foot begins to extend into the hook echo in the latter half of this period just prior to tornadogenesis. The leftward turn of the Z_{DR} arc is owing to a different physical mechanism; a descending reflectivity core (DRC), which is associated with lower values of Z_{DR}, is evident at the leading edge of the FFD at 1955 and 1959 UTC, which shifts the Z_{DR} centroid northward. After the influence of the DRC subsides, the deepest section of the Z_{DR} arc returns to the leading edge of the FFD (especially by 2008 UTC with a depth larger than 1.5 km)

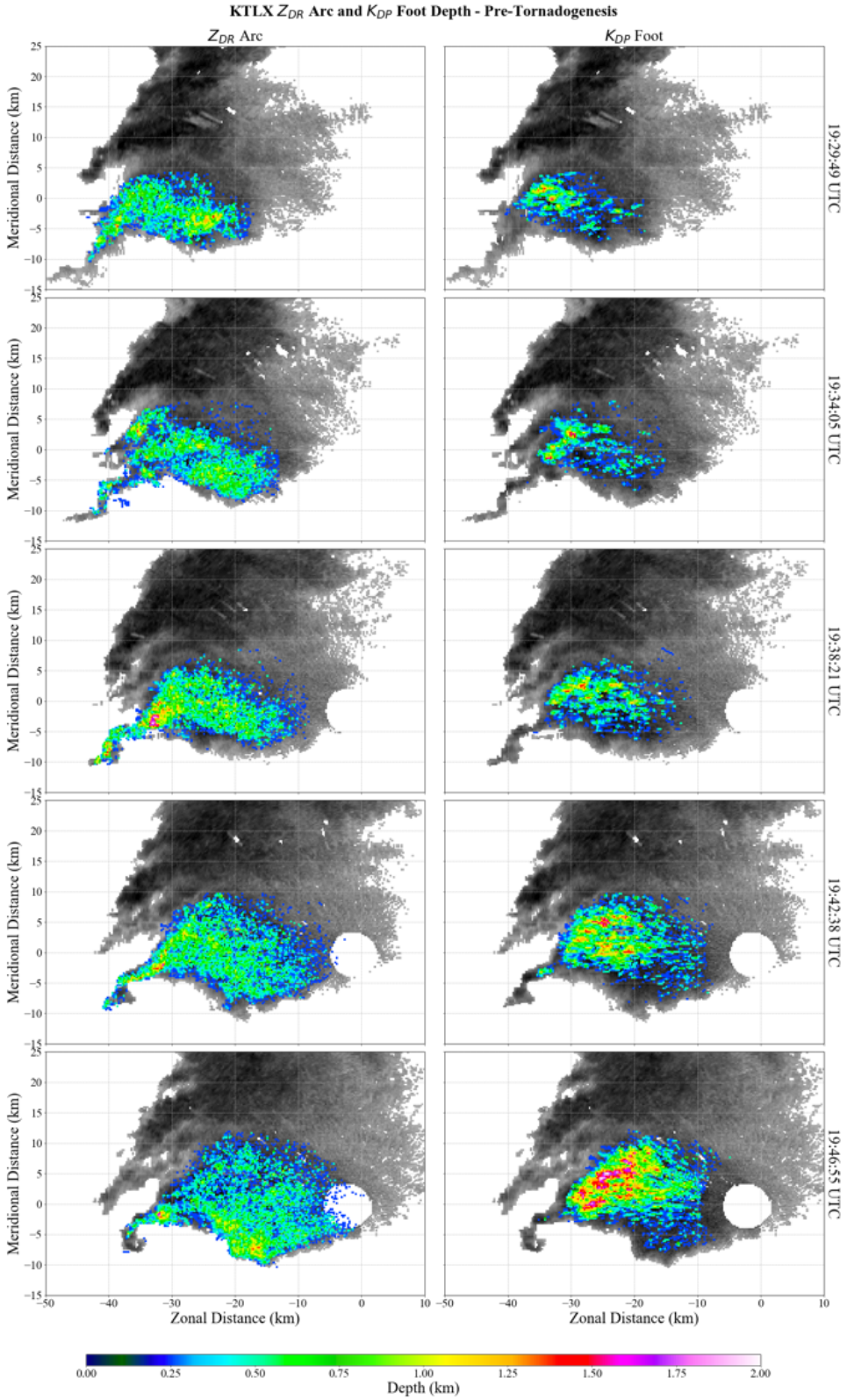

Figure 5.3: Plot of the depth field for Z_{DR} arc and K_{DP} foot from KTLX for five consecutive radar scans from 1929:49 to 1946:55 UTC.

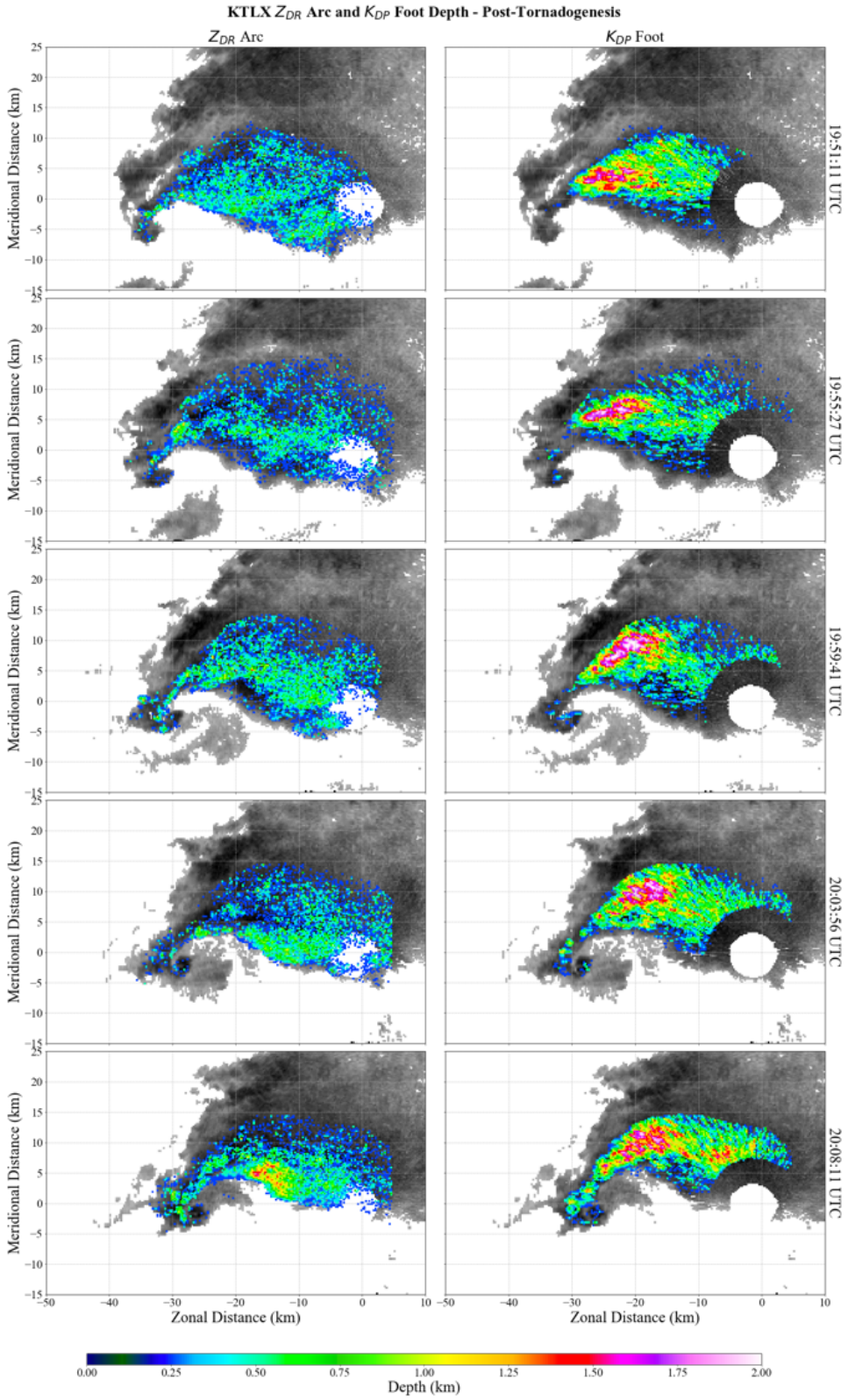

Figure 5.4: As in 5.3, except for scans from 1951:11 to 2008:11 UTC.

and the Z_{DR} arc centroid loses the strong northward movement. During this time period, the separation distance remains relatively steady while the separation distance is characterized by a slight decrease until tornadogenesis followed by a slight increase.

5.2 Z_{DR} and K_{DP} Column

Detection of the Z_{DR} and K_{DP} column relies exclusively on KTLX data since the PX-1000 was collected at only one elevation and KOUN / KCRI are in close proximity to the storm such that at the end of the analysis period, only one elevation (19.8°) is above the 0°C level, making analysis of the columns difficult. Also, recall that data were interpolated to a regular 0.25×0.25×0.5 km grid and that for a data point to count as a column region, the data point must be larger than the respective threshold and above the 0°C level, in this case ∼4.2 km per the 1700 UTC OUN sounding (Figure 4.1). The Z_{DR} and K_{DP} thresholds are 2 dB and 1 ° km^{-1}, respectively. The column depth field at each time is shown in Figure 5.5 and 5.6.

The volumetric extent (column depth) for the Z_{DR} and K_{DP} columns is shown in Figure 5.7a (b). After 1934 UTC and before tornadogenesis, there is a clear trend of decreasing volume and depth in the Z_{DR} column; the only time for which Z_{DR} column volume and depth increases prior to tornadogenesis is at 1943 UTC. On the other hand, trends in K_{DP} column are more variable; volumetric patterns show an increase until 1943 UTC followed by a decrease until 1951 UTC, while depth patterns show a general decrease until 1946 UTC and a slight increasing trend afterwards. The persistent decrease in Z_{DR} column extent just prior to tornadogenesis is consistent

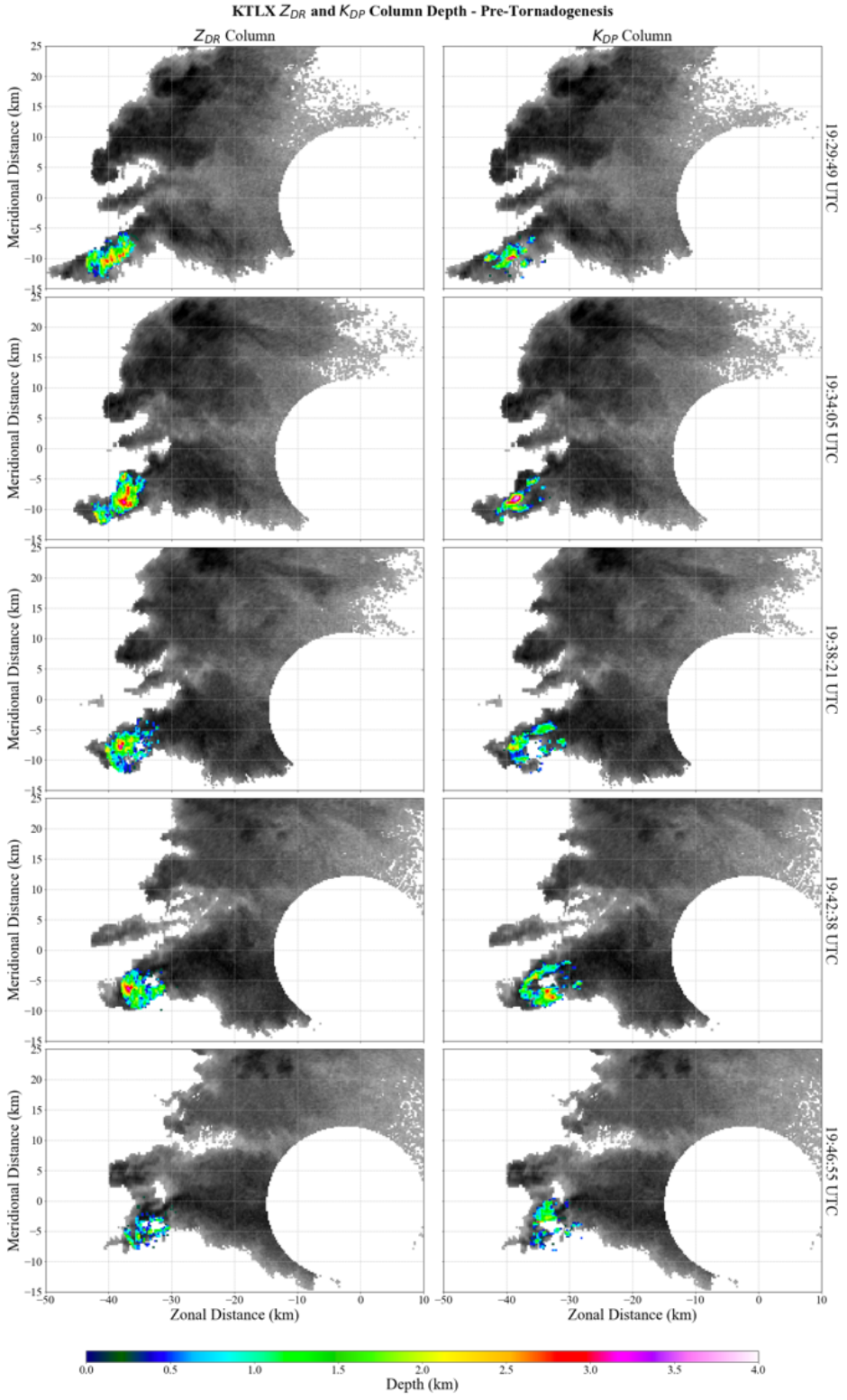

Figure 5.5: Plot of the depth field for Z_{DR} and K_{DP} column from KTLX for five consecutive radar scans from 1929 to 1946 UTC.

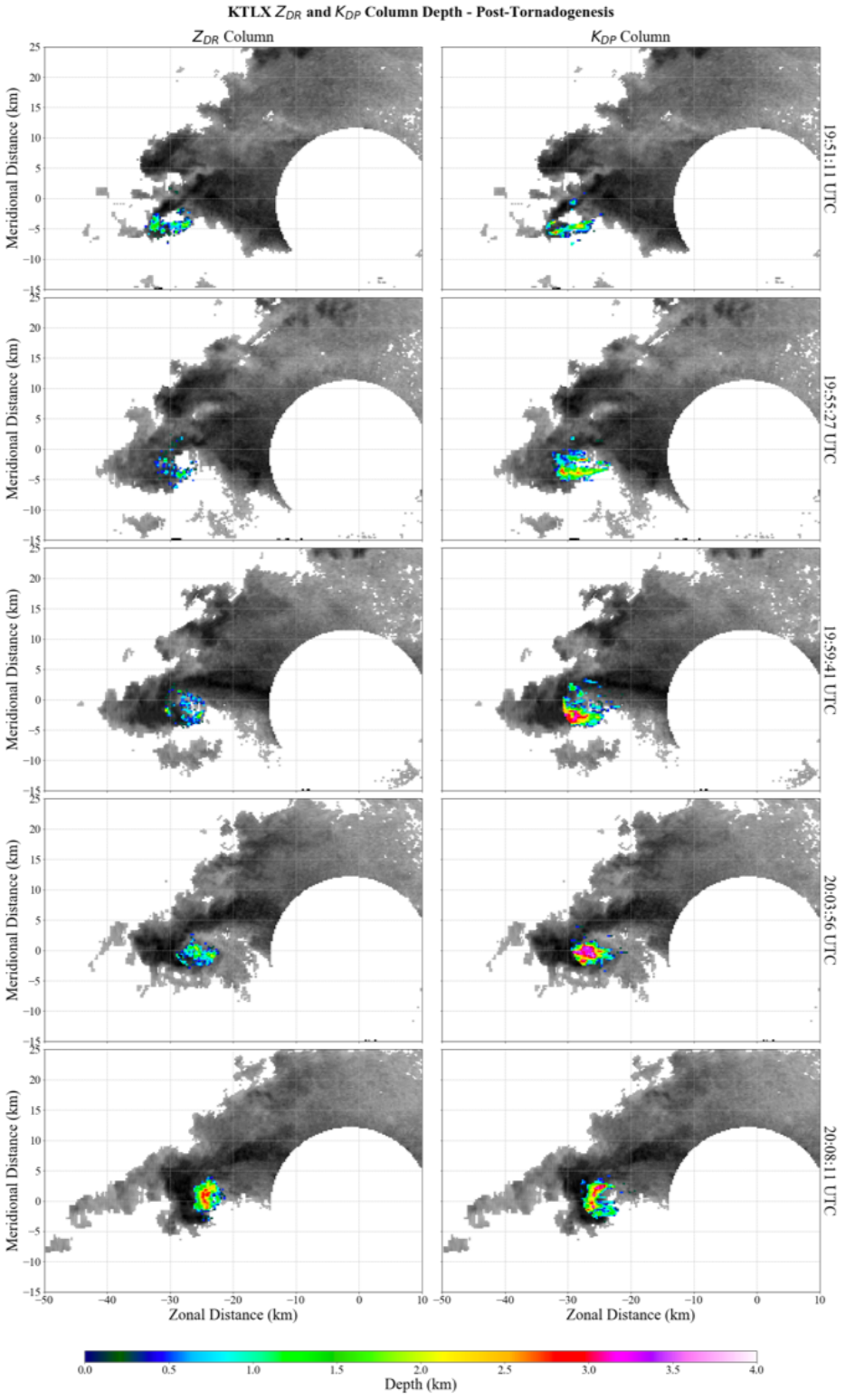

Figure 5.6: As in Figure 5.5, except for scans from 1951 UTC to 2008 UTC.

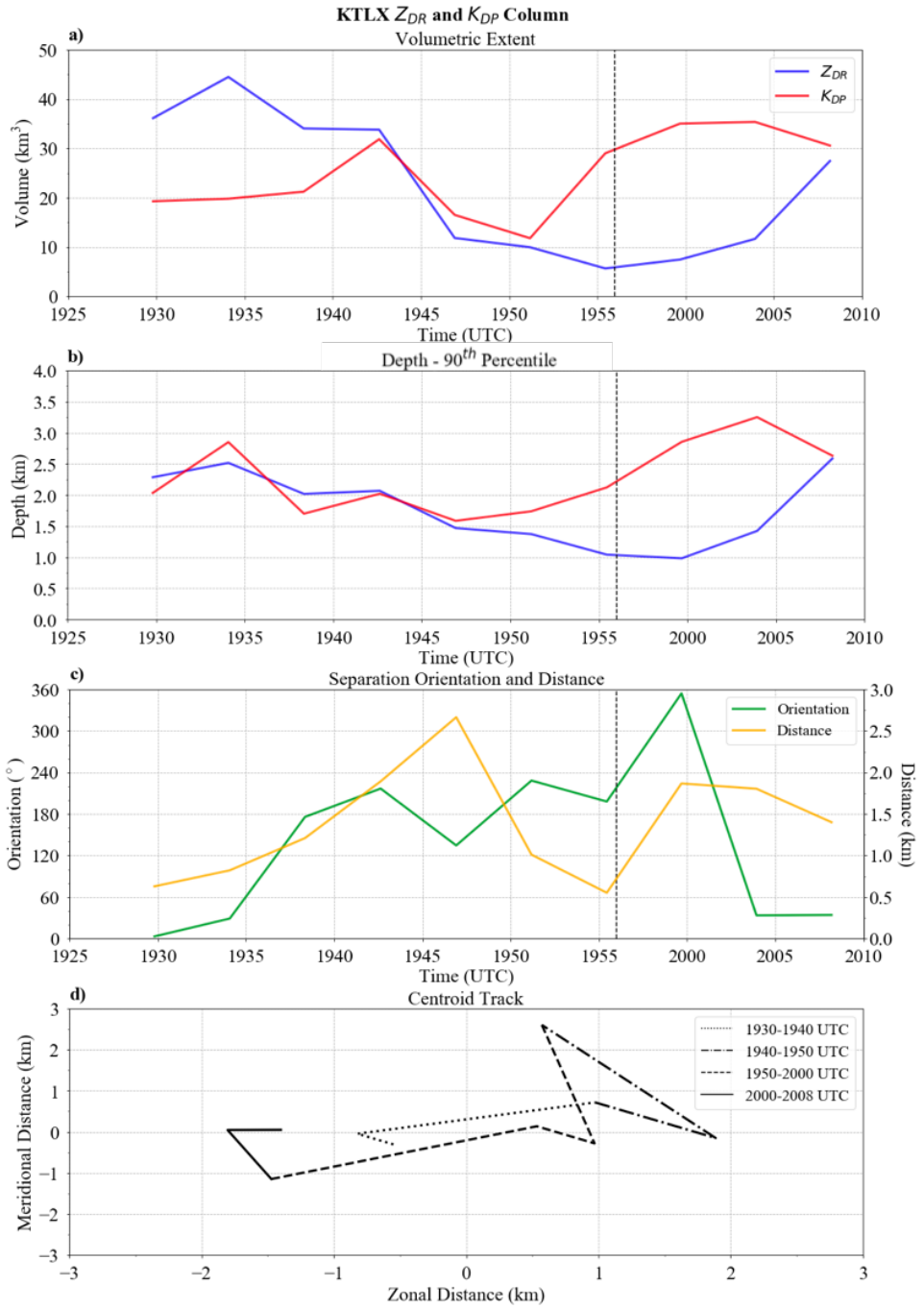

Figure 5.7: a) Volumetric extent of the Z_{DR} and K_{DP} columns, b) 90^{th} percentile of the depth for both columns, c) separation orientation using the centroids, and d) the relative location of the K_{DP} column with respect to the Z_{DR} column.

with previous work (Brandes 1978; Lemon and Doswell 1979; Adlerman et al. 1999; Trapp et al. 1999). As the low- and mid-level mesocyclone intensifies, the downward perturbation pressure gradient force also strengthens, resulting in a weakened updraft and a subsequent decrease in the extent of the Z_{DR} and K_{DP} columns (Picca et al. 2015; Dalman et al. 2018). Moreover, Picca et al. (2015) suggested future studies to compare column trends to trends in low-level rotational velocity as a more direct test of the hypothesis. The column depth field clearly illustrates a decrease in the areal extent of the columns coincident with a decrease in the maximum height of the columns from 1938 to 1946 UTC (Figure 5.5). The most apparent decrease occurs with the Z_{DR} column between 1942 UTC and 1946 UTC, which is simultaneous with transient increases in ΔV_{max} (Figure 4.3) and inferred strengthening of the low-level mesocyclone and increased downward perturbation pressure gradient force. The volumetric minimum in the K_{DP} column occurs at 1951 UTC, which is also coincident with a transient increase in ΔV_{max}.

The exception to the steady decrease before tornadogenesis occurs at 1943 UTC in which there is a local maximum in the K_{DP} column depth and volume along with a leveling off of the Z_{DR} column decrease (Figure 5.7a-b). This is also apparent in the Z_{DR} and K_{DP} column depth field with a brief deepening and increase in areal extent at 1943 UTC, especially notable in the K_{DP} column (Figure 5.5). Stano et al. (2014) utilized a lightning jump algorithm developed by Schultz et al. (2009, 2011) on the 20 May 2013 supercell and observed a reinforcing lightning jump at 1943 UTC. The correlation between an observed lightning jump and an increase in updraft strength

has been well-documented (Schultz et al. 2009, 2011; Gatlin and Goodman 2010, among others).

Additionally, polarimetric data in Chapter 4 confirms that there was also a signal of a near-surface pTDS during this time. Thus, based on the lightning jump and brief increase / leveling off of K_{DP} / Z_{DR} column depth / volume, a brief updraft burst may have occurred about 10 – 15 min prior to tornadogenesis. Therefore, pre-tornadogenesis temporal evolution of Z_{DR} and K_{DP} columns highlights a overarching trend of a weakening updraft along with an embedded brief, but detectable, updraft pulse at 1943 UTC.

Decreasing volumetric extent of both K_{DP} and Z_{DR} columns reverses to growth at 1951 and 1956 UTC, respectively. This volumetric increase is especially notable in K_{DP} column, from approximately 10 km^3 to 35 km^3 at 1951 UTC and 1959 UTC, respectively. The growth of K_{DP} column volume and depth suggests that intensification of vertical velocities and updraft strength associated with the onset of tornadogenesis is enough to overcome negative perturbation pressure gradients that acted to decrease columnar extent prior to tornadogenesis. The explosive growth of the K_{DP} column relative to the Z_{DR} column is likely owing to smaller droplets associated with the former being lofted much faster and higher than larger droplets associated with the latter (Kumjian et al. 2014; Snyder et al. 2017). Moreover, the large influx of small drops into the RFD that are recirculated into the updraft may be a contributing factor, as well as the influence of the storm merger around this time. Figure 5.6 shows the evolution of column depth for Z_{DR} and K_{DP} starting from 1951 UTC and confirms patterns found with volumetric extent. The Z_{DR} column remains relatively steady

until 2003 – 2008 UTC in which there is rapid volumetric growth and deepening of the column. Namely, Figure 5.6 signifies a deepening and consolidation of the Z_{DR} column by 2008 UTC, with a much larger and concentrated region of Z_{DR} column depth greater than 6 km. This time period is coincident with a second intensification period of the tornado from a ΔV_{max} of 70 $\mathrm{m\,s^{-1}}$ to 100+ $\mathrm{m\,s^{-1}}$ K_{DP} column experiences a rapid deepening as well, maximizing at 2003 UTC with a K_{DP} column depth around 3.25 km. Between 2003 – 2008 UTC, both Z_{DR} and K_{DP} column reach their maximum height through the entire observation period.

The same analyses involving the separation distance and orientation between Z_{DR} arc and K_{DP} foot is performed with Z_{DR} and K_{DP} column (Figure 5.7b). While Figure 5.7c–d illustrate fluctuations in the relative positions of the Z_{DR} and K_{DP} column centroid — namely, K_{DP} column located to the east (west) of the Z_{DR} column during the middle (beginning and end) of the analysis period — the fluctuations are relatively small. For example, the largest separation distance through the period is just greater than 2.5 km, and thus these differences in orientation and distance are too small to draw substantial conclusions, which is in contrast to past studies (e.g., Crowe et al. 2012).

Chapter 6

Conclusions and Future Work

Multi-Doppler coverage of a violent, long-track tornado — consisting of radars varying in spatial, temporal, and volumetric capabilities — are sparse in the literature. Combined with the rareness of EF-5 tornadoes, this makes 20 May 2013 an important case to analyze. Conditions on this day were suitable for robust convection, with numerous areas of convective initiation off the dryline in southwest Oklahoma. However, the lack of low-level shear diminished any substantial tornado threat; thus, the boundary associated with the draping cold front evident on KTLX was essential in providing low-level support in initial updraft strengthening / maintenance and likely provided the necessary streamwise vorticity for a violent, long-track tornado. This analysis focused on detailing polarimetric supercell attributes leading up to tornadogenesis and through tornado intensification. Two analyses were conducted to analyze in-storm processes within the supercell – high-spatiotemporal supercell evolution using PX-1000 and volumetric characteristics of Z_{DR} and K_{DP} signatures using KTLX and KOUN, both of which are additionally supplemented with ΔV_{max} and HCA using X- and S-band.

The high-temporal PX-1000 analysis sufficiently resolved three distinct RFD surges that occurred in the period leading up to and during tornadogenesis at 1946:09, 1952:27, and 1957:05 UTC. These surges exhibited an eastward acceleration of the

eastern periphery of the hook echo precipitation region and consisted of identical polarimetric patterns consisting of an advancing Z_H and Z_{DR} gradient wrapping cyclonically around the low-level mesocyclone, a subsequent decrease in ρ_{hv}, and an increase in pTDS points coincident with an intensification in ΔV_{max}. While past studies have noted the importance of DRCs in tornadogenesis and increasing low-level rotation, this is the first study that documents the impact of pulses of precipitation traversing through the hook echo that correlate with increases in low-level rotation. The Z_{DR} gradient results from two different microphysical processes (Kumjian 2011; French et al. 2015), an extension of the Z_{DR} arc into the hook leading to large drops and high Z_{DR} and warm rain processes resulting in small drops and low Z_{DR}. As the RFD surges outwards, intensification of near-surface winds culminating in a local maximum in ΔV_{max} likely lofting small debris, lowering ρ_{hv} and Z_{DR} and contributing to detection of pTDS points from HCA. Most notably, pTDS points associated with the second RFD surge is coincident with a ΔV_{max} greater than 80 $\mathrm{m\,s^{-1}}$ and a prominent number of damage indicators, possibly suggestive of a brief tornado which was unable to sustain itself. Additionally, a large spike in pTDS points and a transient increase in ΔV_{max} occurred just before 1953 UTC; Ortega et al. (2014) also noted a ΔV_{max} increase with confluent damage / tree fall patterns and a debris cloud at this time, further suggesting the presence of a weak, short-lived vortex preceding the long-lived EF-5 tornado.

Because of uncertainties associated with attenuation correction methods, KTLX and KOUN were used to analyze the temporal trends relating to the Z_{DR} arc and K_{DP} foot to ensure consistency in results. This also presented the opportunity to

examine the Z_{DR} arc and K_{DP} foot signatures volumetrically, an analysis that has yet to be done. While both Z_{DR} arc and K_{DP} foot exhibit increasing trends of areal extent, only K_{DP} foot displays significant consolidation / deepening downshear of the updraft. Relative shallowness of the Z_{DR} arc indicates that drop size sorting is occurring in a relatively shallow layer. Additionally, strengthening of the K_{DP} foot and shifting downshear of the updraft prior to tornadogenesis is consistent with Crowe et al. (2012); Loeffler and Kumjian (2018); this shift was further evidenced in the centroid track as a sharp northward turn. The Z_{DR} arc also exhibited a northward turn, albeit not as significant, likely owing to the influence of DRCs within the leading edge of the FFD which are characterized by relatively low Z_{DR}. Regardless, tendencies of the Z_{DR} arc and K_{DP} foot centroid tracks reveal an increase in separation distance and decrease in separation orientation in the times leading up to tornadogenesis, consistent with Loeffler and Kumjian (2018).

The relative distance of KTLX to the supercell compared to KOUN and KCRI also provides the ability to analyze characteristics of the Z_{DR} and K_{DP} column above the 0°C level, which are related to updraft strength. Both volumetric extent and depth of the Z_{DR} and K_{DP} column decrease in the times leading up to tornadogenesis, consistent with Picca et al. (2015) and Dalman et al. (2018). This study quantified low-level rotation to show that this decrease is associated with the strengthening of the low-level mesocyclone and resultant increase in the downward perturbation pressure gradient force (Brandes 1978; Lemon and Doswell 1979; Adlerman et al. 1999; Trapp et al. 1999). The only time in which both the volumetric extent and depth increase prior to tornadogenesis is at 1942:38 UTC, which corresponds with detection of a

surface pTDS from HCA and reinforcing lightning jump at 1943 UTC found in Stano et al. (2014). Simultaneous occurrence of these features insinuates a possible updraft pulse at around 1943 UTC embedded within an overall weakening Z_{DR} and K_{DP} column. Reversal to explosive Z_{DR} and K_{DP} column growth occurs at the time of or after tornadogenesis; volumetric growth of the K_{DP} column occurs especially early and rapidly, possibly linked to an influx of smaller droplets into the updraft correlated with the simultaneous RFD surge captured by PX-1000 and coincident storm merger. Relatively fast growth of the Z_{DR} column is delayed until 2003 – 2008 UTC, which coincides with a post-tornadogenesis ΔV_{max} intensification from 70 to 100 $\mathrm{m\,s^{-1}}$, and may represent a delay in the the influx of larger, heavier drops.

Owing to the availability of volumetric data from KTLX, KOUN, and KCRI, and the high-temporal resolution PX-1000, opportunities for further analyses are abundant. Future work could expand upon the Z_{DR} and K_{DP} analysis presented in this study and extend the analysis period into the mature stages of the tornado through tornado dissipation. Additional characteristics of the updraft, including low-level mesocyclone and vortex tilt, especially during the RFD surges, tornadogenesis, and failed occlusion could be insightful in providing information on tornadogenesis processes. The utilization of supplementary remote sensing instruments, such as satellite, could confirm findings of temporal trends in updraft characteristics using features such as cloud-top temperatures within the overshooting top (Homeyer and Kumjian 2015; Griffin et al. 2016; Bluestein et al. 2019). Finally, characteristics of the surface boundary may also warrant additional investigation considering its likely role in tornadogenesis and maintenance.

Appendix A

HCA Functions

The functions to determine the memberships for S-band HCA as given by Park et al. (2009) are:

$$f_{11} = -0.5 + 2.5 \times 10^{-3} \times 5 + 7.5 \times 10^{-4} \times 5^2$$

$$f_{12} = -0.5 + 2.5 \times 10^{-3} \times 40 + 7.5 \times 10^{-4} \times 40^2$$

$$f_{13} = -0.5 + 2.5 \times 10^{-3} \times 10 + 7.5 \times 10^{-4} \times 10^2$$

$$f_{14} = -0.5 + 2.5 \times 10^{-3} \times 45 + 7.5 \times 10^{-4} \times 45^2$$

$$f_{16} = -0.5 + 2.5 \times 10^{-3} \times 75 + 7.5 \times 10^{-4} \times 75^2$$

$$f_{18} = -0.5 + 2.5 \times 10^{-3} \times 80 + 7.5 \times 10^{-4} \times 80^2$$

$$f_{21} = 0.68 - 4.81 \times 10^{-2} \times 20 + 2.92 \times 10^{-3} \times 20^2$$

$$f_{22} = 0.68 - 4.81 \times 10^{-2} \times 25 + 2.92 \times 10^{-3} \times 25^2$$

$$f_{23} = 0.68 - 4.81 \times 10^{-2} \times 45 + 2.92 \times 10^{-3} \times 45^2$$

$$f_{24} = 0.68 - 4.81 \times 10^{-2} \times 55 + 2.92 \times 10{-}3 \times 55^2$$

$$f_{25} = 0.68 - 4.81 \times 10^{-2} \times 50 + 2.92 \times 10^{-3} \times 50^2$$

$$f_{26} = 0.68 - 4.81 \times 10^{-2} \times 60 + 2.92 \times 10^{-3} \times 60^2$$

$$f_{31} = 1.42 + 6.67 \times 10^{-2} \times 45 + 4.85 \times 10^{-4} \times 45^2$$

$$f_{32} = 1.42 + 6.67 \times 10^{-2} \times 50 + 4.85 \times 10^{-4} \times 50^2$$

and the functions for X-band HCA as given by Snyder et al. (2010) are:

$$A_1 = 3.2 \times 10^{-5} \times Z_H^3 - 0.0017 \times Z_H^2 + 0.042 \times Z_H - 0.39$$

$$A_2 = -4.1 \times 10^{-5} \times Z_H^3 + 0.0059 \times Z_H^2 - 0.096 \times Z_H + 0.49$$

$$A_3 = 4.85 \times 10^{-4} \times Z_H^2 + 6.67 \times 10^{-2} \times Z_H + 1.42$$

Bibliography

Adlerman, E. J., and K. K. Droegemeier, 2005: The dependence of numerically simulated cyclic mesocyclogenesis upon environmental vertical wind shear. *Mon. Wea. Rev.*, **133**, 3595–3623.

Adlerman, E. J., K. K. Droegemeier, and R. Davies-Jones, 1999: A numerical simulation of cyclic mesocyclogenesis. *J. Atmos. Sci.*, **56**, 2045–2069.

Alexander, C. R., and J. Wurman, 2005: The 30 May 1998 Spencer, South Dakota storm. Part I: The structural evolution and environment of the tornadoes. *Mon. Wea. Rev.*, **133**, 72–96.

Atkins, N. T., K. M. Butler, K. R. Flynn, and R. M. Wakimoto, 2014: An integrated damage, visual, and radar analysis of the 2013 Moore, Oklahoma EF5 tornado. *Bull. Amer. Meteor. Soc.*, **95**, 1549–1561.

Bluestein, H. B., M. M. French, R. L. Tanamachi, S. Frasier, K. Hardwick, F. Junyent, and A. Pazmany, 2007a: Close-range observations of tornadoes in supercells made with a dual-polarization, X-band, mobile Doppler radar. *Mon. Wea. Rev.*, **135**, 1522–1543.

Bluestein, H. B., D. T. Lindsey, D. Bikos, D. W. Reif, and Z. B. Weinhoff, 2019: The relationship between overshooting tops in a tornadic supercell and its radar-observed evolution. *Mon. Wea. Rev.*

Bluestein, H. B., C. C. Weiss, M. M. French, E. M. Holthaus, R. L. Tanamachi, S. Frasier, and A. L. Pazmany, 2007b: The structure of tornadoes near Attica, Kansas, on 12 May 2004: High-resolution mobile, Doppler radar observations. *Mon. Wea. Rev.*, **135**, 475–506.

Bluestein, H. B., C. C. Weiss, and A. L. Pazmany, 2004: The vertical structure of a tornado near Happy, Texas, on 5 May 2002: High-resolution, mobile, W-band, Doppler radar observations. *Mon. Wea. Rev.*, **132**, 2325–2337.

Bodine, D., M. R. Kumjian, R. D. Palmer, P. L. Heinselman, and A. V. Ryzhkov, 2013: Tornado damage estimation using polarimetric radar. *Wea. Forecasting*, **28**, 139–158.

Bodine, D. J., R. D. Palmer, and G. Zhang, 2014: Dual-wavelength polarimetric radar analyses of tornadic debris signatures. *J. Appl. Meteor. Climatol.*, **53**, 242–261.

Brandes, E. A., 1978: Mesocyclone evolution and tornadogenesis: Some observations. *Mon. Wea. Rev.*, **106**, 995–1011.

Brandes, E. A., J. Vivekanandan, J. D. Tuttle, and C. J. Kessinger, 1995: A study of thunderstorm microphysics with multi-parameter radar and aircraft observations. *Mon. Wea. Rev.*, **123**, 3129–3143.

Broeke, M. S. V. D., 2017: Polarimetric radar metrics related to tornado life cycles and intensity in supercell storms. *Mon. Wea. Rev.*, **145**, 3671–3686.

Burgess, D., and Coauthors, 2014: 20 May 2013 Moore, Oklahoma tornado: damage survey and analysis. *Wea. Forecasting*, **29**, 1229–1237.

Cheong, B. L., R. Kelley, R. D. Palmer, Y. Zhang, M. Yeary, and T.-Y. Yu, 2013: PX-1000: A solid-state polarimetric X-band weather radar and time–frequency multiplexed waveform for blind range mitigation. *IEEE Trans. Instr. Meas.*, **62**, 3064 – 3072, doi:10.1109/TIM.2013.2270046.

Chilson, P. B., W. F. Frick, P. M. Stepanian, J. R. Shipley, T. H. Kunz, and J. F. Kelly, 2012: Estimating animal densities in the aerosphere using weather radar: to Z or not to Z? *Ecosphere*, **72**.

Conway, J. W., and D. S. Zrnić, 1993: A study of production and hail growth using dual-doppler and multiparameter radars. *Mon. Wea. Rev.*, **121**, 2511–2528.

Crowe, C. C., C. J. Schultz, M. Kumjian, L. D. Carey, and W. A. Petersen, 2012: Use of dual-polarization signatures in diagnosing tornado potential. *Electronic J. Operational Meteor.*, **13**, 57–78.

Dalman, D. M., R. L. Tanamachi, P. E. Saunders, B. L. Cheong, D. Bodine, H. B. Bluestein, and Z. B. Weinhoff, 2018: Cataloging rapid-scan observations of Z_{DR} columns in supercells. *29th Conf. on Severe Local Storms*, Stowe, VT, Amer. Meteor. Soc.

Davies-Jones, R., 2008: Can a descending rain curtain in a supercell instigate tornadogenesis barotropically? *J. Atmos. Sci.*, **65**, 2469–2497.

Dolan, B., and S. A. Rutledge, 2009: A theory-based hydrometeor identification algorithm for X-band polarimetric radars. *J. Atmos. Oceanic Technol.*, **26**, 2071–2088.

Doviak, R. J., and D. S. Zrnić, 1993: *Doppler Radar and Weather Observations*. 2nd ed., Dover Publications, Mineola, New York.

Finley, C. A., and B. D. Lee, 2004: High-resolution mobile mesonet observations of RFD surges in the June 9 Basset, Nebraska supercell during Project ANSWERS 2003. *22nd Conf. on Severe Local Storms*, Hyannis, MA, Amer. Meteor. Soc.

French, M. M., H. B. Bluestein, I. PopStefanija, C. A. Baldi, and R. T. Bluth, 2013: Reexamining the vertical development of tornadic vortex signatures in supercells. *Mon. Wea. Rev.n*, **141**, 4576–4601.

French, M. M., D. W. Burgess, E. R. Mansell, and L. J. Wicker, 2015: Bulk hook echo raindrop sizes retrieved using mobile, polarimetric Doppler radar observations. *J. Appl. Meteor. Climatol.*, **54**, 423–450.

Gatlin, P. N., and S. J. Goodman, 2010: A total lightning trending algorithm to identify severe thunderstorms. *J. Atmos. Oceanic Technol.*, **27**, 3–22.

Griffin, C. B., D. J. Bodine, and R. D. Palmer, 2017: Kinematic and polarimetric radar observations of the 10 May 2010, Moore-Choctaw, Oklahoma tornadic debris signature. *Mon. Wea. Rev.*, **145**, 2723–2741.

Griffin, S. M., K. M. Bedka, and C. S. Velden, 2016: A method for calculating the height of overshooting convective cloud tops using satellite-based IR imager and CloudSat Cloud profiling radar observations. *J. Appl. Meteor. Climatol.*, **55**, 479–491.

Grzych, M. L., B. D. Lee, and C. A. Finley, 2007: Thermodynamic analysis of supercell rear-flank downdrafts from Project ANSWERS. *Mon. Wea. Rev.*, **135**, 240–246.

Hall, M. M., S. M. Cherry, and J. F. Goddard, 1984: Identification of hydrometeors and other targets by dual-polarization radar. *Radio Sci.*, **19**, 132–140.

Hirth, B. D., J. L. Schroeder, and C. C. Weiss, 2008: Surface analysis of the rear-flank downdraft outflow in two tornadic supercells. *Mon. Wea. Rev.*, **136**, 2344–2363.

Homeyer, C. R., and M. R. Kumjian, 2015: Microphysical characteristics of overshooting convection from polarimetric radar observations. *Journal of the Atmospheric Sciences*, **72 (2)**, 870–891, doi:10.1175/JAS-D-13-0388.1, URL `http://dx.doi.org/10.1175/JAS-D-13-0388.1`, `http://dx.doi.org/10.1175/JAS-D-13-0388.1`.

Houser, J. B., 2013: Observations of supercell tornado evolution using a mobile, rapid-scan, X-band radar. Ph.D. thesis, University of Oklahoma.

Houser, J. L., H. B. Bluestein, and J. C. Snyder, 2015: Rapid-scan, polarimetric, Doppler radar observations of tornadogenesis and tornado dissipation in a tornadic supercell: The "El Reno, Oklahoma" storm of 24 May 2011. *Mon. Wea. Rev.*, **143**, 2685–2710.

Hubbert, J., V. N. Bringi, and L. D. Carey, 1998: CSU-CHILL polarimetric measurements from a severe hailstorm in eastern Colorado. *J. Appl. Meteor.*, **37**, 749–755.

Illingworth, A. J., and I. J. Caylor, 1988: Identification of precipitation using dual-polarization radar. *Proc. Cloud Physics Conf.*, Bad Homburg, Fed. Rep. of Germany, 372-377.

Karstens, C. D., W. A. G. Jr., B. D. Lee, and C. A. Finley, 2013: Analysis of tornado-induced tree fall using aerial photography from the Joplin, Missouri, and Tuscaloosa–Birmingham, Alabama, tornadoes of 2011. *Journal of Applied Meteorology and Climatology*, **52**, 1049–1068.

Knox, J. A., and Coauthors, 2013: Tornado debris characteristics and trajectories during the 20 April 2011 super outbreak as determined using social media data. *Bull. Amer. Meteor. Soc.*, **94**, 1371–1380.

Kosiba, K., and J. Wurman, 2010: The three-dimensional axisymmetric wind field structure of the Spencer, South Dakota, 1998 tornado. *J. Atmos. Sci.*, **67**, 3074–3083.

Kumjian, M., 2011: Precipitation properties of supercell hook echoes. *E. Journal Severe Storms Meteor.*, **6 (5)**.

Kumjian, M. R., 2013: Principles and applications of dual-polarization weather radar. Part II: warm- and cold-season applications. *J. Operational Meteor.*, **1**, 243–264.

Kumjian, M. R., A. P. Khain, N. Benmoshe, E. Ilotoviz, A. V. Ryzhkov, and V. T. J. Phillips, 2014: The anatomy in physics of Z_{DR} columns: Investigating a polarimetric radar signature with a spectral bin microphysical model. *J. Appl. Meteor. Climatol.*, **53**, 1820–1843.

Kumjian, M. R., J. C. Picca, S. M. Ganson, A. V. Ryzhkov, and J. Krause, 2010: Polarimetric radar characteristics of large hail. *25th Conf. on Severe Local Storms*, Amer. Meteor. Soc., Ed., Denver, CO.

Kumjian, M. R., and A. V. Ryzhkov, 2008: Polarimetric signatures in supercell thunderstorms. *J. Appl. Meteor. Climatol.*, **48**, 1940–1961.

Kumjian, M. R., and A. V. Ryzhkov, 2009: Storm-relative helicity revealed from polarimetric radar measurements. *J. Atmos. Sci.*, **66**, 667–685.

Kurdzo, J. M., D. J. Bodine, B. L. Cheong, and R. D. Palmer, 2015: High-temporal resolution polarimetric X-band Doppler radar observations of the 20 May 2013 Moore, Oklahoma tornado. *Mon. Wea. Rev., in press.*

Kurdzo, J. M., B. L. Cheong, R. D. Palmer, G. Zhang, and J. B. Meier, 2014: A pulse compression waveform for improved-sensitivity weather radar observations. *J. Atmos. Oceanic Technol.*, **31**, 2713–2731.

Lakshmanan, V., J. Zhang, and K. Howard, 2010: A technique to censor biological echoes in radar reflectivity data. *J. Appl. Meteor. Climatol.*, **49**, 435–462.

Lee, B. D., C. A. Finley, and C. D. Karstens, 2012: The Bowdle, South Dakota, cyclic tornadic supercell of 22 May 2010: Surface analysis of rear-flank downdraft evolution and multiple internal surges. *Mon. Wea. Rev.*, **140**, 3419–3441.

Lei, L., G. Zhang, R. J. Doviak, R. Palmer, B. L. Cheong, M. Xue, Q. Cao, and Y. Li, 2012: Multilag correlation estimators for polarimetric radar measurements in the presence of noise. *J. Atmos. Ocean. Tech.*, **29 (6)**, 772–795, doi:10.1175/JTECH-D-11-00010.1.

Lemon, L. R., and C. A. Doswell, 1979: Severe thunderstorm evolution and mesocyclone structure as related to tornadogenesis. *Mon. Wea. Rev.*, **107**, 1184–1197.

Liu, H., and V. Chandrasekar, 1998: Classification of hydrometeor type based on multiparameter radar measurements. *Int. Conf. on Cloud Physics*, Everett, WA, Amer. Meteor. Soc., 253-256.

Liu, H., and V. Chandrasekar, 2000: Classification of hydrometeor type based on polarimetric radar measurements: Development of fuzzy logic and neuro-fuzzy systems, and in-situ verification. *J. Atmos. Oceanic Technol.*, **17**, 140–164.

Loeffler, S. D., and M. R. Kumjian, 2018: Quantifying the separation of enhanced Z_{DR} and K_{DP} regions in nonsupercell tornadic storms. *Wea. Forecasting*, **33**, 1143–1157.

Loney, M. L., D. S. Zrnić, J. M. Straka, and A. V. Ryzhkov, 2002: Enhanced polarimetric radar signatures above the melting level in a supercell storm. *J. Appl. Meteor.*, **41 (1179-1194)**.

Markowski, P. M., 2002: Hook echoes and rear-flank downdrafts: A review. *Mon. Wea. Rev.*, **130**, 852–876.

Markowski, P. M., E. N. Rasmussen, and J. M. Straka, 1998: The occurence of tornadoes in supercells interacting with boundaries during VORTEX-95. *Wea. Forecasting*, **13**, 852–859.

Markowski, P. M., and Y. P. Richardson, 2009: Tornadogenesis: Our current understanding, forecasting considerations, and questions to guide future research. *Atmos. Research*, **93**, 3–10.

Markowski, P. M., J. M. Straka, and E. N. Rasmussen, 2003: Tornadogenesis resulting from the transport of circulation by a downdraft: Idealized numerical simulations. *J. Atmos. Sci.*, **60**, 795–823.

Marshall, J. S., and W. M. K. Palmer, 1948: The distribution of raindrops with size. *J. Meteor.*, **5**, 165–166.

Mashiko, W., 2016: A numerical study of the 6 May 2012 Tsukuba City supercell tornado. Part II: Mechanisms of tornadogenesis. *Mon. Wea. Rev.*, **144**, 3077–3098.

Maynard, R. H., 1945: Radar and weather. *Journal of Meteorology*, **2**, 214–226.

Ortega, K., and Coauthors, 2014: Damage survey and analysis of the 20 May 2013 Newcastle-Moore EF-5 tornado. *Special Sym. on Severe Local Storms: The Current State of the Science and Understanding Impacts*, Atlanta, GA, Amer. Meteor. Soc.

Palmer, R. D., and Coauthors, 2011: The 10 May 2010 tornado outbreak in central Oklahoma: Potential for new science with high-resolution polarimetric radar. *Bull. Amer. Meteor. Soc.*, **92**, 871–891.

Park, H. S., A. V. Ryzhkov, D. S. Zrnić, and K. Kim, 2009: The hydrometeor classification algorithm for the polarimetric WSR-88D: Description and application to an MCS. *Wea. Forecasting*, **24**, 730–748.

Pazmany, A. L., J. B. Mead, H. B. Bluestein, J. C. Snyder, and J. B. Houser, 2013: A mobile rapid-scanning X-band polarimetric (RaXPol) Doppler radar system. *J. Atmos. Oceanic Technol.*, **30 (7)**, 1398–1413.

Picca, J., M. R. Kumjian, and A. V. Ryzhkov, 2010: Z_{DR} columns as a predictive tool for hail growth and storm evolution. *25th Conf. on Severe Local Storms*, Denver, CO, Amer. Meteor. Soc.

Picca, J. C., J. C. Snyder, and A. V. Ryzhkov, 2015: An observational analysis of Z_{DR} column trends in tornadic supercells. *37th Conf. on Radar Meteor.*, Norman, OK, Amer. Meteor. Soc.

Rasmussen, E. N., 2003: Refined supercell and tornado forecast parameters. *Wea. Forecasting*, **18**, 530–535.

Rasmussen, E. N., and D. O. Blanchard, 1998: A baseline climatology of sounding-derived supercells and tornado forecast parameters. *Wea. Forecasting*, **13**, 1148–1164.

Romine, G. S., D. W. Burgess, and R. B. Wilhelmson, 2008: A dual-polarization-radar-based assessment of the 8 May 2003 Oklahoma City tornado supercell. *Mon. Wea. Rev.*, **136**, 2849–2870.

Ryzhkov, A. V., M. R. Kumjian, S. M. Ganson, and P. Zhang, 2013: Polarimetric radar characteristics of melting hail. Part II: Practical implications. *J. Appl. Meteor. Climatol.*, **52**, 2871–2886.

Ryzhkov, A. V., T. J. Schuur, D. W. Burgess, P. L. Heinselman, S. E. Giangrande, and D. S. Zrnić, 2005a: The joint polarization experiment: Polarmetric rainfall measurements and hydrometeor classification. *Bull. Amer. Meteor. Soc.*, **86**, 809–824.

Ryzhkov, A. V., T. J. Schuur, D. W. Burgess, and D. S. Zrnić, 2005b: Polarimetric tornado detection. *J. Appl. Meteor.*, **44**, 557–570.

Sachidananda, M., and D. S. Zrnić, 1987: Rain rate estimates from differential polarization measurements. *J. Atmos. Ocean. Tech.*, **4**, 588–598.

Schultz, C. J., W. A. Petersen, and L. D. Carey, 2009: preliminary development and evaluation of lightning jump algorithms for the realtime detection of severe weather. *J. Appl. Meteor. Climatol.*, **48**, 2543–2563.

Schultz, C. J., W. A. Petersen, and L. D. Carey, 2011: Lightning and severe weather: A comparison between total and cloud-to-ground lightning trends. *Wea. Forecasting*, **26**, 744–755.

Schuur, T. J., A. V. Ryzhkov, and P. L. Heinselman, 2003: Observations and classification of echoes with the polarimetric WSR-88D radar. Tech. rep., NOAA/National Severe Storms Laboratory.

Skinner, P. S., C. C. Weiss, M. M. French, H. B. Bluestein, P. M. Markowski, and Y. P. Richardson, 2014: VORTEX2 observations of a low-level mesocyclone with multiple internal rear-flank downdraft momentum surges in the 18 May 2010 Dumas, Texas, supercell. *Mon. Wea. Rev.*, **142**, 2935–2960.

Snyder, J. C., and H. B. Bluestein, 2014: Some considerations for the use of high-resolution mobile radar data in tornado intensity determination. *Wea. Forecasting*, **29**, 799 – 827.

Snyder, J. C., H. B. Bluestein, D. T. D. II, and Y. Jung, 2017: Simulations of polarimetric, X-band radar signatures in supercells. Part II: Z_{DR} columns and rings and K_{DP} columns. *J. Appl. Meteor. Climatol.*, **56**, 2001–2026.

Snyder, J. C., H. B. Bluestein, G. Zhang, and S. J. Frasier, 2010: Attenuation correction and hydrometeor classification of high-resolution, X-band, dual-polarized mobile radar measurements in severe convective storms. *J. Atmos. Oceanic Technol.*, **27**, 1979–2001.

Snyder, J. C., and A. V. Ryzhkov, 2015: Automated detection of polarimetric tornadic debris signatures using a hydrometeor classification algorithm. *J. Appl. Meteor. Climatol.*, **54**, 1861–1870.

Stano, G. T., C. J. Schultz, L. D. Carey, D. R. MacGorman, and K. M. Calhoun, 2014: Total lightning observations and tools for the 20 May 2013 Moore, Oklahoma tornadic supercell. *J. Operational Meteor.*, **2**, 71–88.

Thompson, R. L., R. Edwards, J. A. Hart, K. L. Elmore, and P. Markowski, 2003: Close proximity soundings within supercell environments obtained from the Rapid Update Cycle. *Wea. Forecasting*, **18**, 1243–1261.

Thompson, R. L., C. M. Mead, and R. Edwards, 2007: Effective storm-relative helicity and bulk shear in supercell thunderstorm environments. *Weather and Forecasting*, **22 (102-115)**.

Trapp, R. J., E. D. Mitchell, G. A. Tipton, D. W. Effertz, A. I. Watson, D. L. Andra, and M. A. Magsig, 1999: Descending and nondescending tornadic vortex signatures detected by WSR-88Ds. *Wea. Forecasting*, **14**, 625–639.

Umeyama, A., B. L. Cheong, S. Torres, and D. Bodine, 2018: Orientation analysis of simulated tornadic debris. *J. Atmos. Oceanic Technol.*, **35**, 993–1010.

Van Den Broeke, M. S., 2016: Polarimetric variability of classic supercell storms as a function of environment. *Journal of Applied Meteorology and Climatology*, **55**, 1907–1925.

Van Den Broeke, M. S., and S. T. Jauernic, 2014: Spatial and temporal characteristics of polarimetric tornadic debris signatures. *J. Appl. Meteor. Climatol.*, **53 (10)**, 2217–2231.

Vivekanandan, J., S. M. Ellis, R. Oye, D. S. Zrnić, A. V. Ryzhkov, and J. Straka, 1999: Cloud microphysics retrieval using S-band dual-polarization radar measurements. *Bull. Amer. Meteor. Soc.*, **80**, 381 – 388, doi:http://dx.doi.org/10.1175/1520-0477(1999)080<0381:CMRUSB>2.0.CO;2.

Weisman, M. L., and J. B. Klemp, 1982: The dependence of numerically simulated convective storms on vertical wind shear and buoyancy. *Mon. Wea. Rev.*, **110**, 504–520.

Wolff, C., 1998: Radar basics. URL `https://www.radartutorial.eu`.

Wurman, J., D. Dowell, Y. Richardson, P. Markowski, E. Rasmussen, D. Burgess, L. Wicker, and H. B. Bluestein, 2012: The Second Verification of the Origins of Rotation in Tornadoes Experiment: VORTEX2. *Bull. Amer. Meteor. Soc.*, **93**, 1147 – 1170.

Wurman, J., and K. Kosiba, 2013: Finescale radar observations of tornadoes and mesocyclone structures. *Wea. Forecasting*, **28**, 1157 – 1174.

Wurman, J., K. Kosiba, and P. Robinson, 2013: In situ, Doppler radar, and video observations of the interior structure of a tornado and the wind-damage relationship. *Bull. Amer. Meteor. Soc.*, **94**, 835–846.

Zrnić, D. S., A. Ryzhkov, J. Straka, Y. Liu, and J. Vivekanandan, 2001: Testing a procedure for automatic classification of hydrometeor types. *J. Atmos. Oceanic Technol.*, **18**, 892–913.